Journal of Hazardous Materials 391 (2020) 122163

Contents lists available at ScienceDirect

Journal of Hazardous Materials

journal homepage: www.elsevier.com/locate/jhazmat

Direct synthesis of nitrogen-doped mesoporous carbons from triazine-functionalized resol for CO_2 uptake and highly efficient removal of dyes

Ahmed F.M. EL-Mahdy[a], Tzu-En Liu[a], Shiao-Wei Kuo[a,b,*]

[a] Department of Materials and Optoelectronic Science, Center of Crystal Research, National Sun Yat-Sen University, Kaohsiung, 80424, Taiwan
[b] Department of Medicinal and Applied Chemistry, Kaohsiung Medical University, Kaohsiung, 807, Taiwan

GRAPHICAL ABSTRACT

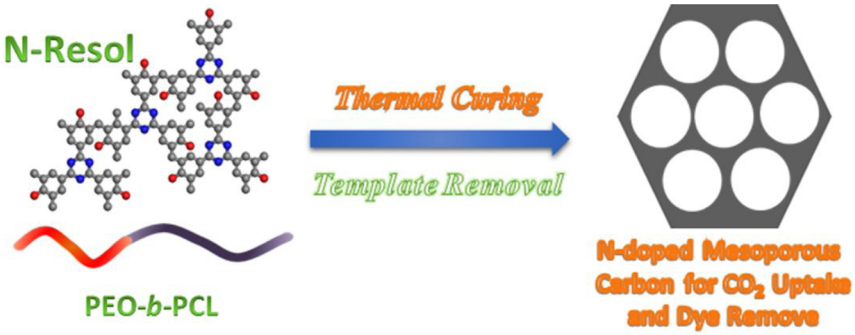

ARTICLE INFO

Editor: Rinklebe Jörg

Keywords:
Triazine–formaldehyde phenolic resin
N-doped mesoporous carbon
Block copolymer
CO_2uptake
Organic dye adsorption

ABSTRACT

In this study we synthesized a triazine–formaldehyde phenolic resin as a nitrogen-containing resol (N-resol) through the condensation of 2,4,6-tris(4-hydroxyphenyl)triazine and formaldehyde. We then used this N-resol as a carbon and nitrogen atom source, mixing it with a diblock copolymer of PEO-*b*-PCL as the soft template, for the direct synthesis of N-doped mesoporous carbons. Interestingly, the self-assembled N-resol/PEO-*b*-PCL blends underwent a mesophase transition from cylinder to gyroid and back again to cylinder structures upon increasing the N-resol concentration (i.e., cylinder at 50/50; gyroid at 60/40; cylinder at 70/30). After removing the soft template at 700 °C, the resultant N-doped mesoporous carbons possessed high N atom contents (up to 13 wt%) and displayed gyroid and cylinder nanostructures. The synthesized N-doped mesoporous carbons exhibited excellent CO_2 uptake capacities (up to 72 and 150 mg g^{-1} at 298 and 273 K, respectively). Furthermore, the N-doped mesoporous gyroid carbon structure displayed high adsorption capacities toward organic dyes in water. The maximum adsorption capacities of rhodamine B and methylene blue in water reached as high as 204.08 and 308.64 mg g^{-1}, respectively; furthermore, these N-doped mesoporous carbons also maintained up to 98 % of their maximum adsorption capacities within 45 min.

1. Introduction

The colored dyes used extensively in, for example, prints, papers, textiles, and plastics generally display excellent thermal and chemical stabilities (Gupta and Suhas, 2009; Forgacs et al., 2004). Wastewater produced from pharmaceutical, industrial, and biochemical activities

* Corresponding author at: Department of Materials and Optoelectronic Science, Center of Crystal Research, National Sun Yat-Sen University, Kaohsiung 80424, Taiwan.
E-mail address: kuosw@faculty.nsysu.edu.tw (S.-W. Kuo).

https://doi.org/10.1016/j.jhazmat.2020.122163
Received 1 December 2019; Received in revised form 19 January 2020; Accepted 21 January 2020
Available online 06 February 2020
0304-3894/

are often contaminated with dyes, causing inevitable damage to living creatures and the environment. Many kinds of dyes, even at small doses, are toxic to aquatic life, very difficult to biodegrade, and extremely carcinogenic along the biological chain (Adeyemo et al., 2012; Tsai et al., 2007). In addition, small amounts of these dyes can color large blocks of water, causing extensive reflection of sunlight and the high consumption of dissolved O_2, potentially destroying ecosystems and enhancing the growth of bacteria (Allen and Koumanova, 2005). Among the many approaches (e.g., photocatalysis, electrolysis, ion exchange) that have been tested to remove organic dyes from wastewater (Wang et al., 2014), adsorption methods are among the most eco-friendly and effective methods. Several adsorbent materials are commercially available or laboratory-tested, including activated carbons, clay materials, zeolites, and mesoporous silicas and titanium oxide (Rivera-Utrilla et al., 2011; Rafatullah et al., 2010; Lu et al., 2016; Wu et al., 2016). In particular, activated carbons have extremely high adsorption capacities toward most dye molecules, and can also be involved in the catalytic processes of their degradation (Rivera-Utrilla et al., 2011; Gu et al., 2013; Wang et al., 2012; Mezohegyi et al., 2012; Mohammadi et al., 2011). The porosity and surface heteroatoms of the activated carbons are mainly responsible for their adsorption efficiency toward organic dyes (Smith and Rodrigues, 2015). Microporous carbons, which typically have pore sizes of approximately 1–2 nm, exhibit low dye adsorption because most dyes are organic bulky molecules having average dimensions greater than 1 nm and, therefore, the dyes tend to block the pores of such activated carbons. Accordingly, mesoporous carbons (pore sizes: ca. 2–50 nm) are more suitable for removing dyes from wastewater (Dong et al., 2013; Peng et al., 2014; Zhai et al., 2011), with ordered-pore-size mesoporous carbons being more effective than amorphous-pore-size mesoporous carbons. The ordered arrangement of their pores, narrow pore size distributions, high pore volumes, and tunable pore structures of ordered mesoporous carbons all result in their faster adsorption, greater efficiency, and superior selectivity in various applications when compared with those of other reported mesoporous materials (Liang et al., 2008; Lee et al., 2006).

Recently, microporous carbons have been prepared by using various methods. For example, metal-organic frameworks (MOFs)-derived carbons which prepared by the calcination of zeolitic imidazolate framework (ZIF) (Li et al., 2018; Kaneti et al., 2017), biomass-derived carbon materials which prepared from natural cellulose and bacterial cellulose (Dutta et al., 2017, 2014). On the other hand, soft and hard templating strategies have been allied for the preparation of mesoporous carbons having narrow pore size distributions and well-ordered pore structures. A hard templating method employs pre-designed templates as hard models for the replication of mesoporous carbon materials (Kosonen et al., 2002). It requires the pre-design and synthesis of the hard template, which might be costly, cumbersome, time-consuming, and not suitable for large-scale production (Liu et al., 2018a,b; Mun et al., 2018; Lu et al., 2018; Wang et al., 2018). Through this method, the porosity of the resulting mesoporous carbon is determined mainly by the template. A soft templating method involves the insertion of a block copolymer or organic species through supramolecular self-assembly in the presence of certain organic molecules. With this method, the porosity of the mesoporous carbon is determined by the preparation conditions—for example, the choice of solvent, the mixing ratio, or the temperature. For this present study, we have used a soft templating method because of its time efficiency, simplicity, and ease of removal of the template through thermal treatment (Li et al., 2019; Chu et al., 2017; Li et al., 2011; Liu et al., 2014a, b; Lee et al., 2014; Hu et al., 2010).

Recently, nitrogen (*N*)-doped carbons and related materials have utilized in many applications such as energy storage [electrochemical supercapacitors and sensors, batteries, and fuel cells] and catalysis in organic synthesis reactions and hydrogen evolution reactions due to their promising properties (Mori et al., 2018; Rao and Pramoda, 2019; Zhao et al., 2019; Yasukawa and Kobayashi, 2019). As new kinds of N-doped carbons, N-doped mesoporous carbons have received much attention due to their excellent chemical, physical, mechanical, and electronic properties (Shen and Fan, 2013). The incorporation of N atoms into a mesoporous carbon material can improve the surface polarity, electronic conductivity, and electron donor tendency, in addition to its performance in various applications (Guo et al., 2017; A.B. Chen et al., 2015; T. Chen et al., 2015). In terms of dye removal, a few papers have demonstrated the ability of N-doped mesoporous carbons to remove organic dyes from wastewater (Liu et al., 2014a, b; Sánchez-Sánchez et al., 2015; Li et al., 2016; Liang et al., 2016; Jiao et al., 2017). For example, Hu et al. reported that the N-doped mesoporous carbon CMK-3 exhibited an uptake efficiency of anionic dyes (including methyl orange) that was stronger than that of microporous carbons; this effect was attributed to the ordered pore size of CMK-3 and the electron-donating effect of the incorporation of the N atoms. Nitrogen-doped mesoporous carbons can be prepared using either post-synthesis or soft-templating methods. The former involves the impregnation of mesoporous carbons with melamine, polypyrrole, or urea, followed by exposure to NH_3 gas under an inert atmosphere (Deng et al., 2016; Lee et al., 2013; Wei et al. (2012); Chen et al., 2012); this method can, however, be complex, costly for practical application, and time-consuming. The soft-templating approach generally involves the use of phenolic resin as a carbon source, a block copolymer as a template, and a N-functionalized organic species as a source of N atoms. The OH groups of the resol network structure coordinate to the copolymer through hydrogen bonds; the mesoporous material is then obtained after removing the copolymer through calcination. Wei et al. prepared N-doped mesoporous carbons using the soft-templating method, with phenol-formaldehyde resol as the carbon source, dicyandiamide as the N atom source, and the Pluronic F-127 block copolymer as the template. The resol and dicyandiamide were assembled into micelles of the F-127 copolymer, stabilized by electrostatic interactions and hydrogen bonds; subsequent evaporation-induced self-assembly (EISA) and thermal annealing (to remove the template, provided a N-doped mesoporous carbon having a high N atom content (13.1 wt%) and tunable pore size and mesostructure (Wei et al., 2013a,b). Yu et al. also reported the preparation of a N-doped mesoporous carbon when using Pluronic F127 as the template, urea as the N atom source, hexamethylenetetramine as a slow-release source of formaldehyde, and resorcinol–formaldehyde resol as the carbon source. Co-assembly of these four components under hydrothermal conditions provided a N-doped mesoporous carbon having a N atom content of 2.5 wt% (Yu et al., 2014). Bayatsarmadi et al. synthesized N-doped mesoporous spherical carbons when using a mixture of F-127 and the fluorocarbon FC4 as the soft template, with melamine and resorcinol–formaldehyde resol as N and C atom sources, respectively. The resultant carbon materials had N atom contents of 25.7–5.5 wt% (Bayatsarmadi et al., 2015). The block copolymer PEO-*b*-PCL has been used as a soft template, along with phenol–formaldehyde resol and melamine, for the preparation of a N-doped mesoporous carbon having a N atom content of 2.8 wt% (Chu et al., 2017). Similarly, the block copolymer poly(styrene–*b*–acrylic acid) (PS-*b*-PAA) has been used as a soft template, with urea–formaldehyde precursor as the C and N atom source, for the synthesis of a N-doped mesoporous carbon having a N atom content of 19 wt% (Liu et al., 2018a,b).

The examples discussed above reveal that the use of N-functionalized resol polymers as sources of both C and N atoms has been limited and uncommon. To the best of our knowledge, the synthesis of N-containing resol polymers based on N-rich triazine moieties has not been reported previously. In this study, we report the synthesis of a triazine–formaldehyde phenolic resol through the simple condensation of 2,4,6-tris(4-hydroxyphenyl)triazine (THPT) and formaldehyde in the presence of NaOH (Scheme 1). We then prepared a series of N-doped mesoporous carbons having gyroid and cylinder nanostructures by using the triazine–formaldehyde resol as a C and N atom source and the simple diblock copolymer PEO-*b*-PCL as a soft template (Scheme 2). We

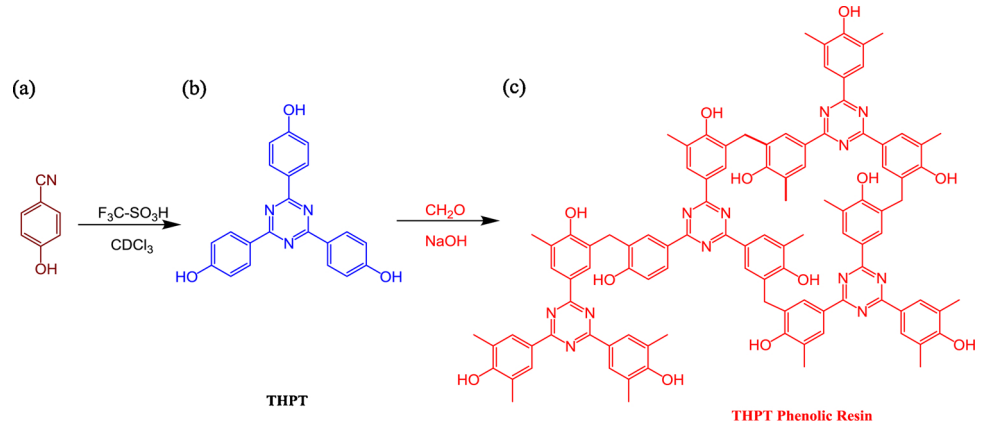

Scheme 1. (a) Structure of the commercially available 4-cyanophenol. (b, c) synthesis of (b) THPT and (c) the N-containing resol phenolic resin (N-Resol).

applied a variety of analytical techniques to study the characteristics of these samples, including Fourier transform infrared (FTIR) spectroscopy, nuclear magnetic resonance (NMR) spectroscopy, differential scanning calorimetry (DSC), thermogravimetric analysis (TGA), small-angle X-ray scattering (SAXS), transmission electron microscopy (TEM), and N_2 sorption isotherms. Because of their N-rich structures, the synthesized mesoporous carbons exhibited excellent CO_2 uptake ability and superior efficiency for the removal of the dyes rhodamine B (RhB) and methylene blue (MB) from water.

2. Experimental section

2.1. Materials

ε-Caprolactone monomer was purchased from Acros and purified through vacuum distillation over CaH_2. Monomethoxy-poly(ethylene glycol) (M_n =5000 g/mol; Fluka) was used as a macro-initiator to synthesize the PEO-*b*-PCL diblock copolymer (M_n = 16,000 g/mol; PDI = 1.27) through ring-opening polymerization, with stannous(II) octoate [$Sn(Oct)_2$] as the catalyst (Chu et al., 2017; Li and Kuo, 2011; Su et al., 2019; Chu et al., 2016, 2014). ^1H and ^{13}C NMR spectra and GPC traces of the prepared PEO-*b*-PCL diblock copolymer are provided in Figs S1–S3. RhB and MB were obtained from TCI. 4-Cyanophenol, trifluoromethanesulfonic acid (TfOH), and paraformaldehyde were also purchased from Acros.

2.2. 2,4,6-tri-(4-hydroxyphenyl) Triazine (THPT) (Abuzeid et al., 2019)

A solution of 4-cyanophenol [Scheme 1(a); 2.00 g, 16.8 mmol) in $CHCl_3$ (40 mL) in a double-necked flask was stirred under N_2 in an ice bath. TfOH (7.6 mL) was added carefully over a period of 1 h and then the ice bath was removed and the mixture warmed to room temperature over 18 h. Distilled H_2O (50 mL) was added and then the mixture was neutralized with 2 M NH_4OH until the pH was greater than 7 to produce a precipitate. The precipitate was collected and placed in a vacuum oven at 100 °C, giving an off-white solid [1.86 g, 93 %; Scheme 1(b)]. FTIR (KBr, cm^{-1}): 3545–3120, 1143, 1633, 1579, 1500, 3029, 3045. ^1H NMR (500 MHz, DMSO-d_6, ppm): δ 10.28 (s, 3 H), 8.54 (d, J =9.0 Hz, 6 H), 6.97 (d, J =8.5 Hz, 6 H). ^{13}C NMR (125 MHz, DMSO-d_6, ppm): δ 205.91, 171.46, 161.93, 131.65, 128.68, 115.99.

2.3. Nitrogen-containing resol phenolic resin (N-Resol resin)

A solution of THPT (0.5 g), formaldehyde (1.4 mL), and NaOH (0.05 g) in dioxane (3 mL) was heated at 100 °C under a N_2 atmosphere for 1 h. The mixture was neutralized with HCl and then the solvents were distilled off under reduced pressure. Tetrahydrofuran (THF) was added and then the mixture was subjected to centrifugation. The liquid phase was concentrated to obtain the N-resol [Scheme 1(c)]. FTIR (KBr, cm^{-1}): 3680-3079, 2977-2850, 1608, 1526, 1434, 1356, 1269, 1242, 1110, 1023, 811. ^1H NMR (500 MHz, DMSO-d_6, ppm): δ 9.55 (s, aromatic OH, 12 H), 8.55 (d, J =8.5 Hz, 24 H), 6.98 (d, J =8.5 Hz, 13 H), 5.77 (s, aliphatic OH, 13 H), 4.67-4.56 (m, CH_2O, 48 H), 3.61-3.27 (m, CH_2, 10

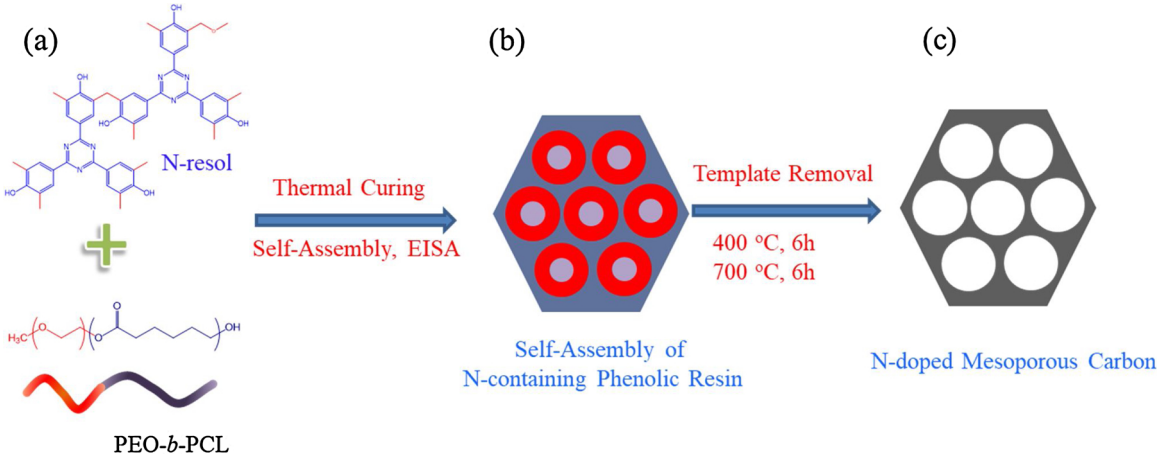

Scheme 2. Schematic representation of the direct synthesis of N-doped mesoporous carbon structures: (a) blending of N-resol and PEO-*b*-PCL, (b) self-assembly of mixtures of N-resol/PEO-*b*-PCL through EISA and thermal curing, and (c) removal of the template through heating at 400 °C for 6 h and then at 700 °C for 6 h under a N_2 atmosphere.

H). ^{13}C NMR (125 MHz, DMSO-d_6, ppm): δ 170.91, 162.91, 131.26, 129.36, 127.18, 116.16, 89.26, 84.50, 82.32, 67.61, 30.98.

2.4. Direct synthesis of N-Doped mesoporous carbon

A mixture of PEO-*b*-PCL and N-resol resin (various amounts of each) in THF was stirred until they had dissolved completely. The solution was then poured into an aluminum pan and the THF was evaporated at room temperature slowly over 24 h through EISA, followed by heating to 150 °C for 24 h to complete the thermal curing. Pyrolysis of the block copolymer was performed at 400 °C for 6 h. Furthermore, pyrolysis of the N-containing mesoporous phenolic resin was performed 700 °C for 6 h in a tubular furnace under a N_2 atmosphere to provide the N-doped mesoporous carbon (Scheme 2).

2.5. Dye adsorption experiments

Two organic dyes—RhB and MB—were selected to study the efficiency of the carbon material to remove dyes from water. In a typical experiment, N-doped mesoporous carbon (5 mg) was added to an aqueous solution of the dye (RhB or MB, 10 mL) in a glass vial and then the mixture was stirred (for 0, 15, 30, 45, 60, or 90 min) at a rate of 500 rpm. The supernatant was then isolated through centrifugation (6000 rpm, 10 min). The UV–Vis spectrum of the isolated supernatant was measured. To obtain adsorption isothermal curves, various concentrations of the aqueous dye (from 12.5 to 150 mg L^{-1}) were used. For each test, the N-doped mesoporous carbon (2 mg) was added to an aqueous solution of the dye (10 mL) in a glass vial and then the mixture was stirred (500 rpm) for 24 h. The supernatant was isolated through centrifugation and its UV–Vis spectrum recorded, to construct the isothermal curve. Adsorption reusability tests were performed by adding the N-doped mesoporous carbon (3 mg) to an aqueous solution of the dye (25 mg L^{-1}; 10 mL) and then stirring for 1 h. The supernatant was isolated and its UV–Vis spectrum recorded. The N-doped mesoporous carbon was washed several times with H_2O, EtOH, THF, and acetone to remove the adsorbed dye. After drying the carbon material overnight at 100 °C, it was used in the next dye removal test. The adsorption isothermals of RhB and MB were fitted using the Langmuir isothermal model (linear form), expressed as follows:

$$\frac{C_e}{Q_e} = \frac{1}{K_L Q_m} + \frac{C_e}{Q_m}$$

where C_e (mg L^{-1}) is the equilibrium dye concentration in the liquid phase; Q_e (mg g^{-1}) is the equilibrium adsorption of dye per unit mass of the adsorbent carbon; Q_m (mg g^{-1}) is the maximum equilibrium adsorption of dye per unit mass of the adsorbent carbon; and $\mathbf{K}_L$ (L mg^{-1}) is the Langmuir constant.

2.6. Characterization

FTIR spectroscopy was performed from 4000 to 400 cm^{-1} using a Bruker Tensor 27 spectrophotometer. ^{1}H and ^{13}C NMR spectroscopy was performed using a Bruker 500 (500 MHz) spectrometer at 25 °C, with DMSO-d_6 and $CDCl_3$ as internal standards. TGA of the N-resol was performed using a TA Q-50 TGA analyzer; the sample was heated from 40 to 800 °C under a N_2 atmosphere at a heating rate of 20 °C min^{-1}. DSC analyses of the samples were performed using a TA Q-20 DSC apparatus; the sample (3 mg) was placed in an aluminum pan and heated from –40 to +100 °C under a N_2 atmosphere at a heating rate of 20 °C min^{-1}. SAXS of the assembled N-resol/PEO-*b*-PCL blends and N-doped mesoporous carbons was performed at the BL17B3 beamline [wavelength (λ): 1.24 Å] of the National Synchrotron Radiation Research Center (NSRRC), Taiwan. TEM images of the blends and carbons were recorded using a JEOL-JEM-2100 microscope operated at 200 kV. The N_2 sorption isotherms and CO_2 uptakes of the N-doped mesoporous carbons were measured using an ASAP 2020 analyzer; the samples were activated at 100 °C for 12 h prior to measurement. The pore size distributions of the samples were calculated using the non-local density functional theory (NLDFT). UV–Vis–NIR spectra were recorded at 25 °C using a Jasco V-570 spectrometer, with deionized water as the solvent. Raman spectra were recorded at 25 °C using a Jobin-Yvon T6400 micro Raman apparatus, with a He–Cd laser (325 nm line) as an excitation source.

3. Results and discussion

3.1. Synthesis of N-Resol resin

We synthesized a new phenolic triazine–formaldehyde resol (N-resol) containing N-rich triazine moiety through the simple condensation of THPT and formaldehyde solution (37 %) in dioxane at 100 °C for 1 h under a N_2 atmosphere (Scheme 1). The chemical structure of the new N-resol was confirmed using FTIR and ^{1}H and ^{13}C NMR spectroscopy. The FTIR spectrum of N-resol (Fig. S4) featured a broad signal from 3671 to 3010 cm^{-1}, representing the stretching of phenolic OH groups, in addition to two signals at 1603 and 1529 cm^{-1}, representing the vibrations of aromatic C=C bonds. The ^{1}H NMR spectrum of N-resol in DMSO-d_6 featured [Fig. 1(a)] small signals at 9.56 and 5.78 ppm, attributable to its phenolic and aliphatic OH groups, respectively. The aromatic protons were represented by two strong signals at 8.52 and 6.97 ppm. Typically, phenol–formaldehyde resol resins contain several kinds of CH_2 groups, including those bridging aromatic rings, those in methylol groups, and those of ether groups (Panamgama and Pizzi 1995; Werstler, 1986; Sojka et al., 1979). Similarly, the ^{1}H NMR spectrum of our N-resol featured several signals in the range from 4.79 to 4.49 ppm, representing methylol (PhC$\underline{H}_2$OH, PhCH$_2$OC$\underline{H}_2$OH,

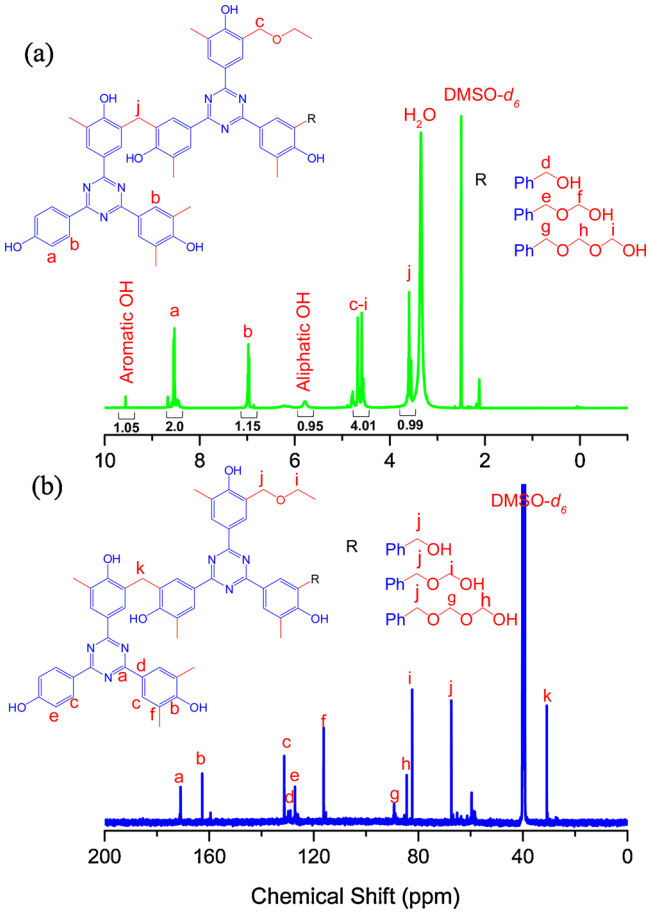

Fig. 1. (a) ^{1}H and (b) ^{13}C NMR spectra of N-resol.

$PhCH_2OCH_2O\underline{CH_2}OH$) and methylene ether ($PhC\underline{H_2}OCH_2OH$, $PhC\underline{H_2}OC\underline{H_2}OCH_2OH$) units, as well as a signal for the methylene bridge ($PhC\underline{H_2}Ph$) at 3.58 ppm. The ^{13}C NMR spectrum of N-resol [Fig. 1(b)] featured signals for the triazine C═N and phenolic CO−H atoms at 170.52 and 162.77 ppm, respectively. The aromatic carbon nuclei were represented by signals at 131.13, 129.13, 127.29, and 115.77 ppm. In addition, the methylol $PhC\underline{H_2}OH$, ($PhCH_2O\underline{CH_2}OH$, $PhCH_2OCH_2O\underline{CH_2}OH$) carbon nuclei provided signals at 83.94 and 82.79 ppm. The carbon nuclei of the methylene ether units ($PhC\underline{H_2}OCH_2OH$, $PhC\underline{H_2}O\underline{CH_2}OCH_2OH$) appeared as signals at 88.64 and 67.33 ppm. We attribute the signal at 30.81 ppm to the $PhC\underline{H_2}Ph$ carbon nuclei. The molecular weight of the synthesized N-resol, determined through GPC, was approximately 2300 g mol^{-1}, with the polydispersity index (PDI) of 1.06 (Fig. S5). TGA analysis of the N-resol revealed its excellent thermal stability, with 10 % weight loss occurring after heating at 388 °C and a char yield of 56 wt.% after heating at 800 °C under a N_2 atmosphere (Fig. S6).

3.2. Preparation and physical properties of N-Resol/PEO-b-PCL blends

We used DSC and FTIR spectroscopy to study the thermal behavior, hydrogen bonding, and self-assembly of mixtures of N-resol and PEO-*b*-PCL at various N-resol concentrations. In general, the melting and crystallization temperatures of a polymer can be determined through DSC by measuring the second heating and first cooling scans. The crystallization temperature is usually used as an indicator of any self-assembly or microphase transitions in a block copolymer (Li et al., 2011; Chen et al., 2009). Fig. 2 presents the DSC analyses of N-resol/PEO-*b*-PCL blends: their second heating scans [Fig. 2(a)] and their first cooling scans [Fig. 2(b)]. The glass transition temperature (T_g) of the pure N-resol phenolic resin used in this study was 46 °C; the melting temperatures of the PEO and PCL block segments were similar (ca. 60 °C), as displayed in Fig. 2(a). In addition, pure PEO and PCL block segments exhibited two crystallization temperatures of 36 and 29 °C, respectively, as displayed in Fig. 2(b) (Li and Kuo, 2011). The melting [Fig. 2(a)] and crystallization [Fig. 2(b)] temperatures of the PEO and PCL segments both shifted to lower temperatures upon increasing the concentration of the N-resol phenolic resin, due to a decrease in the chemical potential and a change in the morphology as a result of hydrogen bonding with the N-resol. Furthermore, the crystallization behavior of both the PEO and PCL block segments disappeared when the N-resol resin content was 70 wt%, as displayed in Fig. 2(b).

We used FTIR spectroscopy to study the hydrogen bonding interactions in the N-resol/PEO-*b*-PCL blends (Fig. 3). The C═O units of PCL and the C−OC− units of PEO underwent intermolecular hydrogen bonding with the N-resol phenolic resin, as expected. In previous studies, we calculated the inter-association equilibrium constant (K_A = 264) of the phenolic/PEO binary pair to be higher than that (K_A = 116) of the phenolic/PCL binary pair (Kuo et al., 2002; Kuo, 2018). Fig. 3(a) and 3(b) present the C═O and COC−− stretching regions, respectively, of the N-resol/PEO-*b*-PCL blends. The C−OC− stretching region, in the range 1000 − 1140 cm^{-1}, is displayed in Fig. 3(b). The spectrum of pure PEO-*b*-PCL exhibited a characteristic band at 1108 cm^{-1} for the free ether units of the PEO segment; this signal shifted to 1095 cm^{-1} upon the addition of the N-resol phenolic resin at all compositions, the result of hydrogen bonding of the N-resol with the PEO segment. The signals of the C═O units in the range of 1680–1780 cm^{-1} are displayed in Fig. 3(a). The spectrum of pure PEO-*b*-PCL exhibits characteristic bands at 1734 and 1724 cm^{-1}, corresponding to the amorphous (or free) and crystalline PCL segments, respectively. The intensity of the signal of the crystalline PCL conformation at 1724 cm^{-1} decreased, and an additional absorption band appeared at 1708 cm^{-1}, due to the hydrogen-bonded C═O units, upon increasing the concentration of the N-resol resin. Thus, the N-resol OH units interacted with both the PEO and PCL segments when the N-resol resin concentration was higher than 60 wt %, consistent with the disappearance of the crystallization temperature from the DSC traces.

We recorded SAXS patterns and TEM images of the N-resol/PEO-*b*-PCL blends after thermal curing to examine their self-assembled nanostructures (Fig. 4). We suspected that the pure PEO-*b*-PCL would display a lamellar crystalline structure, based on its SAXS pattern (peak ratio of 1:2) and TEM image (Kuo, 2018). When the N-resol resin was present at 50 wt%, Fig. 4(a) indicates the long-range order of a cylinder structure, with the SAXS pattern revealing a peak ratio of 1:√3:√4:√7 and the first peak appearing at a value of q^* of 0.272 nm^{-1} (d = 23.25 nm). An hexagonally packed cylinder structure was confirmed using TEM [Fig. 4(b), top view; Fig. 4(c), side view]. Increasing the N-resol resin content to 60 wt%, Fig. 4(d) reveals a double-gyroid structure, with SAXS analysis providing a peak ratio of √6:√8:√16:√20 and the first peak appearing at a value of √6q^* of 0.287 nm^{-1} (d = 21.88 nm);

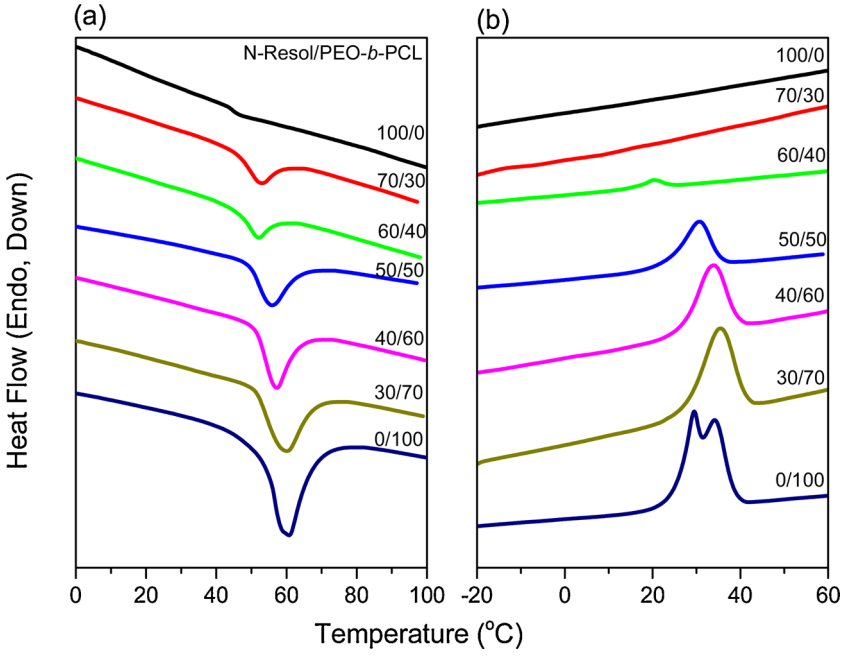

Fig. 2. DSC (a) heating and (b) cooling thermograms of mixtures of N-resol/PEO-*b*-PCL at various N-resol concentrations.

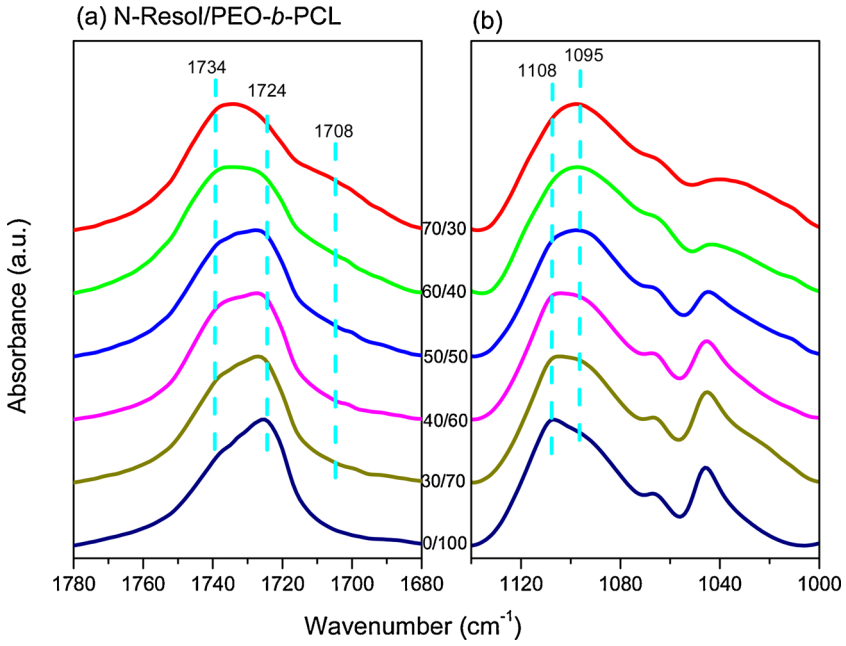

Fig. 3. FTIR spectra of mixtures of N-resol/PEO-*b*-PCL at various N-resol concentrations: (a) carbonyl (C = O) region; (b) ether (C–O) region.

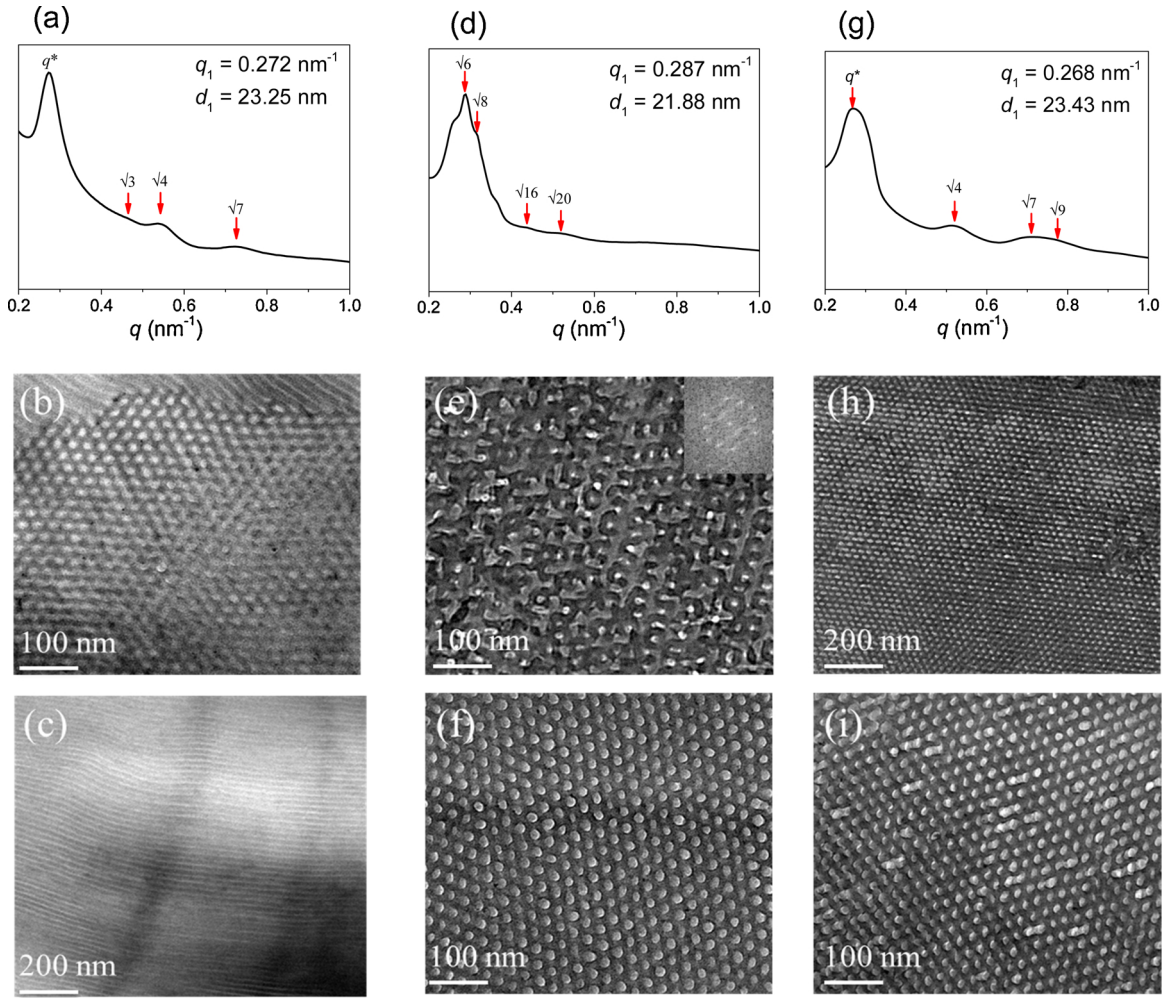

Fig. 4. (a, d, g) SAXS patterns and (b, c, e, f, h, i) TEM images of self-assembled mixtures of N-resol/PEO-*b*-PCL at various N-resol concentrations: (a–c) 50/50, (d–f) 60/40, and (g–i) 70/30.

this structure was also confirmed through TEM {Fig. 4(e), from [211] plane; Fig. 4(f), from [110] plane}. Alter further increasing the N-resol resin content to 70 wt%, Fig. 4(g) reveals the long-range order of a cylinder structure had formed again, with SAXS analysis providing a peak ratio of 1:√4:√7:√9 and the first peak appearing at a value of q^* of 0.268 nm^{-1} (d =23.43 nm), again confirmed through TEM [Fig. 4(h) and 4(i)]. The samples featuring N-resol contents of 30 and 40 wt% were also subjected to SAXS analyses (Fig. S7), but only broad peaks were observed for these two composites, indicating disordered structures, consistent with our previous finding that a lower phenolic resin content did not result in a long-range-ordered self-assembled structure templated by the block copolymer PEO-*b*-PCL (Li et al., 2011). Based on these DSC, FTIR spectral, SAXS, and TEM analyses, the intermolecular hydrogen bonding of N-resol/PEO was stronger than that of N-resol/PCL and, thus, the self-assembly of N-resol/PEO-*b*-PCL blends would occur with competing hydrogen bonding interactions and the PCL block segment would possess phase-separation from miscible N-resol/PEO domain through the reaction-induced microphase separation, as displayed in Scheme 2(b).

3.3. Characterization of N-Doped mesoporous carbon

After thermal curing, we applied further calcination to remove the PEO-*b*-PCL template and obtain the N-doped mesoporous carbon directly (Scheme 2(c)). Figs. 5(a), 5(d), and 5(g) display the SAXS analyses of the N-doped mesoporous carbons obtained after thermal calcination of the N-resol/PEO-*b*-PCL = 50/50, 60/40, and 70/30 blends, respectively. The SAXS signals became sharper with more highly ordered diffraction peaks upon removal of the PEO-*b*-PCL template, because pore formation would lead to a greater difference in electron density. In addition, the first peak in the SAXS pattern was shifted to a lower value of q after thermal calcination, presumably because of thermal expansion. For example, the d-spacings ranged from 23.25 to 30.78 nm for the N-doped mesoporous carbon obtained from the N-resol/PEO-*b*-PCL = 50/50 blend system; furthermore, we observe a similar peak ratio of 1:√3:√4:√7 in Fig. 5(a), also indicating hexagonally packed cylinders. TEM images [top view, Fig. 5(b); side view, Fig. 5(c)] confirmed the mesoporous cylindrical structure, which also featured another short-range ordered structure (e.g., a slit-shaped porous structure). Fig. 5(d) presents the SAXS pattern of the N-doped mesoporous carbon obtained from the N-resol/PEO-*b*-PCL = 60/40 blend system; it indicates the long-range order of a mesoporous double-gyroid structure with a peak ratio of √6:√8:√10:√14:√22:√38:√50, as confirmed through TEM imaging {Fig. 45(e) from [110] plane; Fig. 5(f) from the [211] plane}. Increasing the N-resol resin content to 70 wt% resulted in the long-range order of a mesoporous cylinder carbon, with a peak ratio of 1:√3:√4:√7, as presented in Fig. 5(g); this structure was confirmed by the TEM images in Figs. 5(h) and 5(i).

We recorded N_2 sorption isotherms to further characterize these mesoporous structures (Fig. 6). We observed typical type-IV curves with the relative pressure ranging from 0.45 to 0.95 for the N-doped mesoporous carbons obtained from the N-resol/PEO-b-PCL = 50/50 and 70/

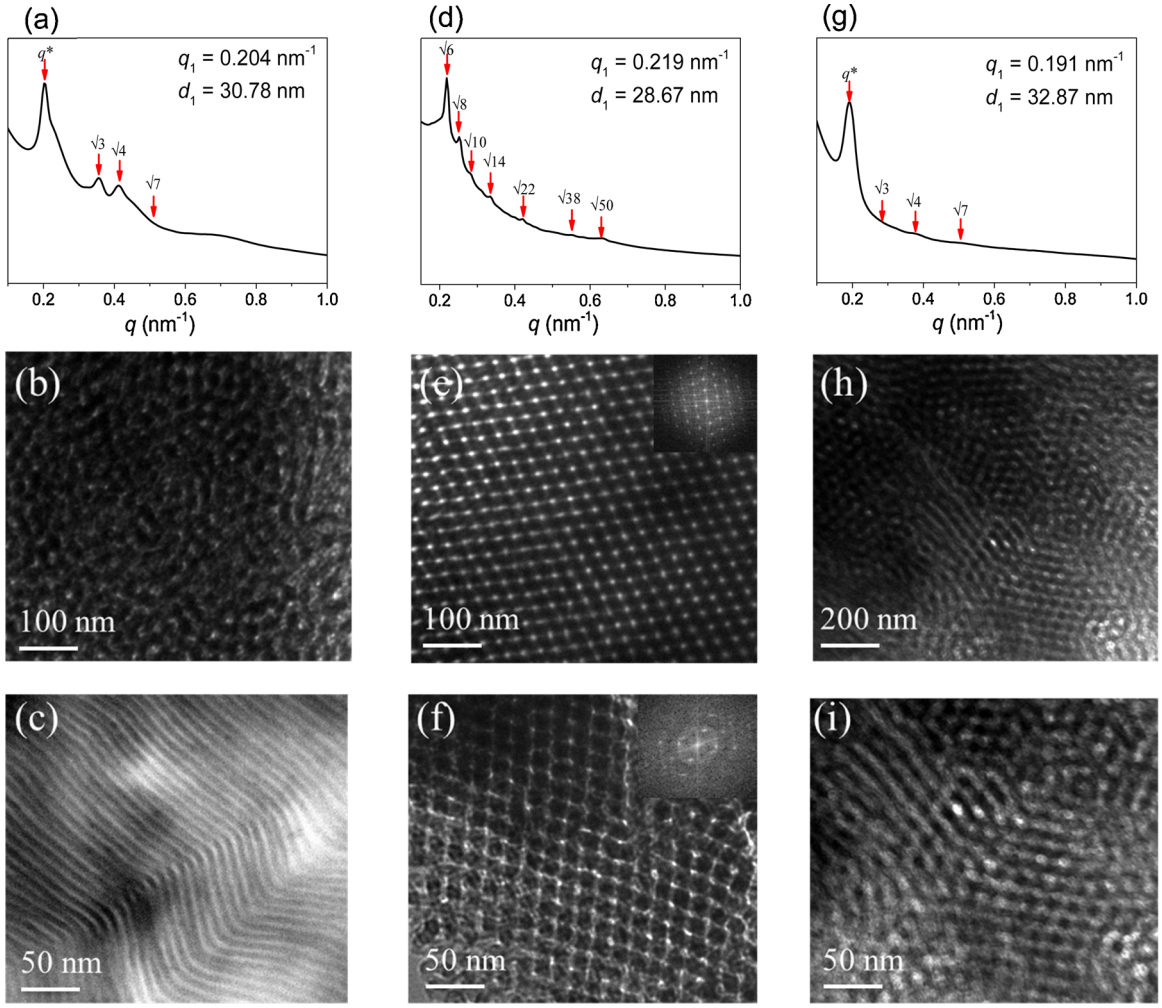

Fig. 5. (a, d, g) SAXS patterns and (b, c, e, f, h, i) TEM images of N-doped mesoporous carbons obtained after calcination of self-assembled mixtures of N-resol/PEO-*b*-PCL at various N-resol concentrations: (a–c) 50/50, (d–f) 60/40, and (g–i) 70/30.

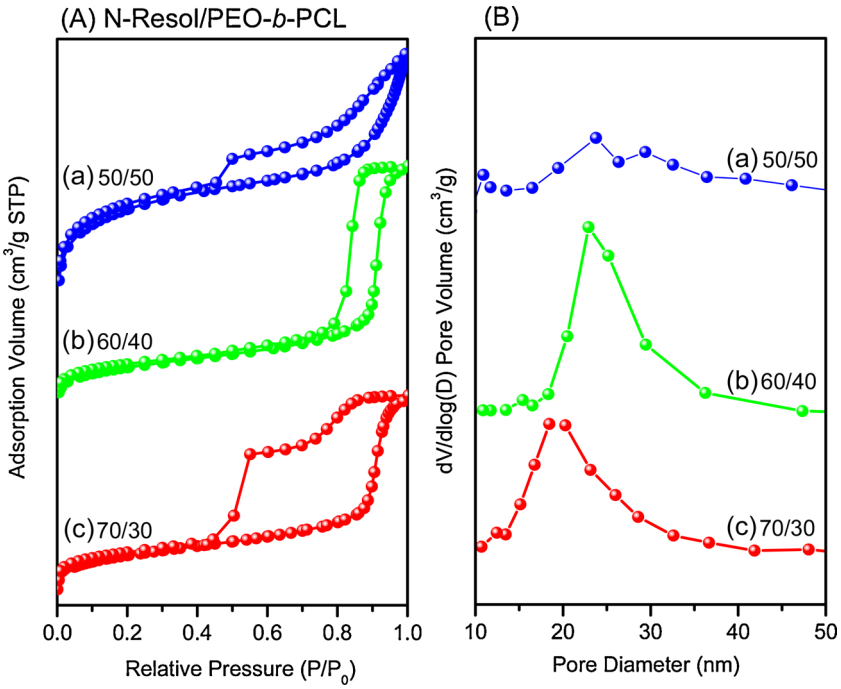

Fig. 6. (A) Nitrogen adsorption/desorption isotherms and (B) NLDFT pore size distributions of N-doped mesoporous carbons obtained after calcination of self-assembled mixtures of N-resol/PEO-*b*-PCL at various N-resol concentrations.

Table 1
BET, SAXS, and Raman spectral data of N-doped mesoporous carbons prepared from self-assembled mixtures of N-resol/PEO-*b*-PCL at various N-resol concentrations.

Sample	S_{BET} ($m^2\ g^{-1}$)	S_{meso} ($m^2\ g^{-1}$)	S_{total} rate	V_{total} ($cm^3\ g^{-1}$)	V_{mseo} ($cm^3\ g^{-1}$)	V_{mseo} rate	Pore size (nm)	*d*-spacing (nm)	I_D/I_G
50/50	610	128	20.98 %	0.3916	0.1512	38.61 %	—	30.78	1.24
60/40	539	191	35.43 %	0.6902	0.5162	74.78 %	23	28.67	1.30
70/30	491	119	24.23 %	0.6108	0.3180	52.06 %	19	32.87	1.17

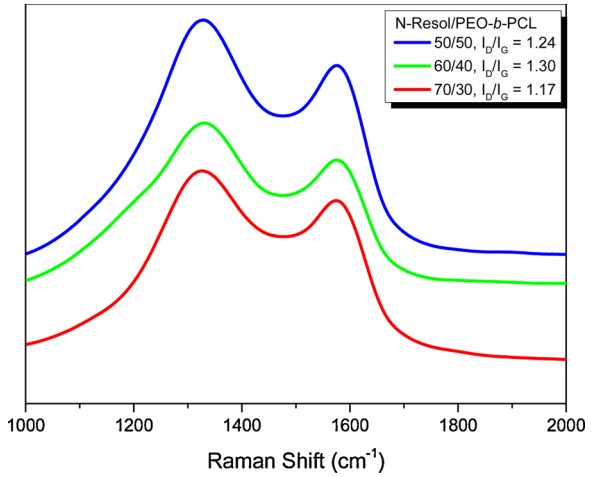

Fig. 7. Raman spectra of N-doped mesoporous carbons obtained after calcination of self-assembled mixtures of N-resol/PEO-*b*-PCL at various N-resol concentrations.

30 blend systems and from 0.85 to 0.95 for the N-doped mesoporous carbons obtained from the N-resol/PEO-b-PCL = 60/40 system, as displayed in Fig. 6(A), suggesting a common mesoporous structure. Fig. 6(A)-(a) displays a H_3-like hysteresis curve, suggesting a slit-shaped porous structure having a broad pore size distribution, as displayed in Fig. 6(B)-(a) for the N-doped mesoporous carbon obtained from the N-resol/PEO-*b*-PCL = 50/50 blend system, consistent with the TEM images in Figs. 5(b) and 5(c). Figs. 6(A)-(b) and 6(A)-(c) reveal H_1-like hysteresis, suggesting well-defined gyroid and cylinder pore channels with narrow pore size distributions (ca. 23 and 19 nm), as displayed in Figs. 6(B)-(b) and 6(B)-(c) for the N-doped mesoporous carbons obtained from the N-resol/PEO-*b*-PCL = 60/40 and 70/30 blend systems, consistent with the TEM images in Figs. 5(e) and 5(f) for the double-gyroid structure and Figs. 5(h) and 5(i) for the cylindrical mesoporous structure. Table 1 summarizes the Brunauer–Emmett–Teller (BET) surface areas, mesoporous surface areas, total pore volumes, and mesoporous pore volumes of our three N-doped mesoporous carbons; our ordered (cylinder and gyroid) structures featured high percentages of their mesoporous structures. In addition, among our samples, the N-doped mesoporous cylinder carbon obtained from the N-resol/PEO-*b*-PCL = 50/50 system possessed the highest BET surface area (610 $m^2\ g^{-1}$); the N-doped mesoporous gyroid carbon and the N-doped mesoporous cylinder carbon obtained from the N-resol/PEO-*b*-PCL = 60/40 and 70/30 blend systems possessed BET surface areas of 539 and 491 $m^2\ g^{-1}$, respectively. However, the highest mesoporous surface area, total pore volume of the N-doped mesoporous gyroid carbon from the N-resol/PEO-*b*-PCL = 60/40 system over than that of the N-doped mesoporous cylinder carbons (50/50 and 70/30 blends) due to its bi-continuous double gyroid mesoporous structure as compared with the cylinder structure as mentioned in previous study. (Li et al., 2019)

Fig. 7 displays the Raman spectra (from 1000 to 2000 cm^{-1}) of the N-doped mesoporous carbons prepared in this study. Two strong bands appeared: one near 1326 cm^{-1} for the D band, corresponding to disordered carbon, and the other near 1575 cm^{-1} for the G band, corresponding to graphitic-carbonized structures. The I_D/I_G ratios of the N-

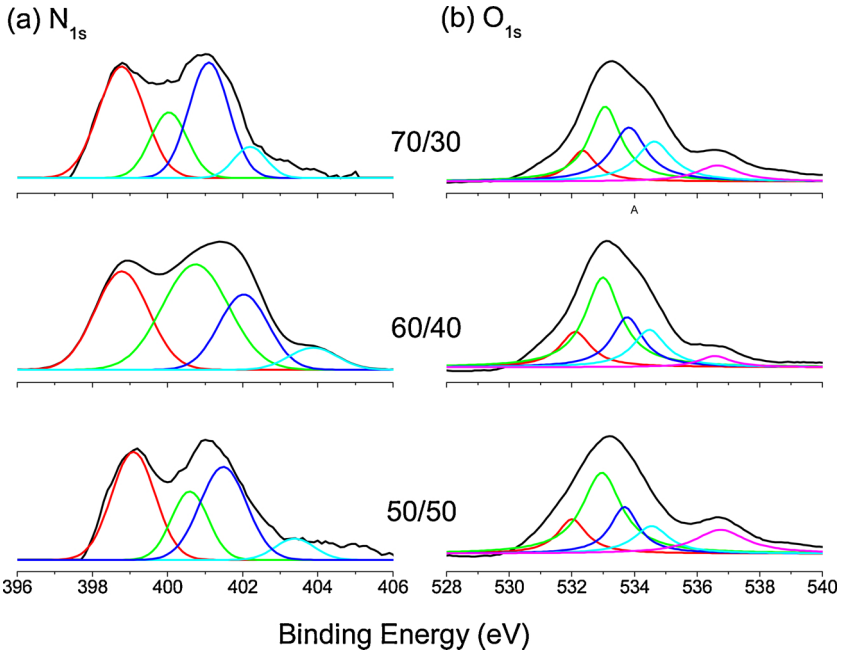

Fig. 8. Fitting of the (a) N 1s and (b) O 1s XPS spectra of N-doped mesoporous carbons.

doped mesoporous carbons obtained from the N-resol/PEO-*b*-PCL = 50/50, 60/40, and 70/30 systems were 1.24, 1.30, and 1.17, respectively, indicating that the most defected structure was that obtained from the N-resol/PEO-*b*-PCL = 60/40 system. Table 1 summarizes the *d*-spacings, pore sizes, pore volumes, and Raman spectral data of these N-doped mesoporous carbons. The N-doped mesoporous double-gyroid carbon obtained from the N-resol/PEO-*b*-PCL = 60/40 system possessed the largest pores (23 nm), the highest mesoporous volume ratio (74.78 %), and the highest I_D/I_G ratio (1.30).

Our N-doped mesoporous carbons provided two characteristic peaks near 400 and 530 eV in their XPS analyses, corresponding to the N_{1s} orbitals of the triazine units (Fig. 8(a)) and the O_{1s} orbitals of the phenolic OH and absorbed water [Fig. 8(b)]. The N-doped mesoporous gyroid carbon possessed the highest N atom content (13 %); in comparison, the N-doped mesoporous cylinder carbons obtained from the N-resol/PEO-*b*-PCL = 50/50 and 70/30 systems possessed N atom contents of 11.5 and 12 %, respectively. Table 2 summarizes the fitting results of Fig. 8 and reveals several types of N and O units in these N doped mesoporous carbons. There were four major types of N_{1s} species: pyridinic-N at 398.8 eV (N-6), pyrrolic-N at 400.5 eV (N-5), quaternary-N at 401.5 eV (N–Q), and oxidized N at 403.4 eV (N-X), as displayed in Fig. 8(a). In addition, there were five major types of O_{1s} species: adsorbed H_2O at 535.9 eV, C − OH at 534.2 eV, C–O at 533.3 eV, C = O at 532.3 eV, and quinone at 531.3 eV, as displayed in Fig. 8(b). The fractions of N-5 and N-6 units and the fractions of C = O and C–OH units in the N-doped mesoporous double-gyroid carbon (obtained from the N-resol/PEO-*b*-PCL = 60/40 system) were the highest (Table 2), suggesting that it might have the greatest potential for dye removal or CO_2 capture.

3.4. CO_2 capture of N-Doped mesoporous carbons

Because of the high N atom contents and surface areas of our synthesized N-doped mesoporous carbons, we tested them for their suitability in two environmentally important applications: CO_2 uptake and the removal of dyes from wastewater. First, we investigated the CO_2 uptake capacities of our carbon materials at 298 and 273 K and up to 1 bar (Figs. 9a and 9b, respectively). Among these new samples, the N-doped mesoporous gyroid carbon exhibited the highest CO_2 capacities: 70 and 150 mg g^{-1} at 298 and 273 K, respectively. The N-doped mesoporous cylinder carbon obtained from the N-resol/PEO-*b*-PCL = 70/30 system provided CO_2 capacities of 66 and 141 mg g^{-1} at 298 and 273 K, respectively; the N-doped mesoporous cylinder carbon formed with the N-resol/PEO-*b*-PCL = 50/50 system displayed the lowest CO_2 capacities: 58 and 125 mg g^{-1} at 298 and 273 K, respectively. We attribute the higher CO_2 uptake efficiencies of the N-doped mesoporous gyroid carbon, relative to those of the cylinder carbons, mainly to the higher N atom content within the gyroid carbons. These N atoms have very high ability to interact with CO_2 molecules and, thus, their presence strongly enhances the CO_2 uptake. Interestingly, the CO_2 uptakes of our synthesized N-doped mesoporous carbons are among the highest ever reported (Wan et al., 2015a,b, Wan et al., 2015a,b; Hao et al., 2010; Wei et al., 2013a,b; A.B. Chen et al., 2015; T. Chen et al., 2015; Bai et al., 2014; Sevilla and Fuertes, 2011; Liu et al., 2017). In comparison with other porous materials such as covalent organic frameworks (EL-Mahdy et al., 2019a,b; EL-Mahdy et al., 2019a,b; EL-Mahdy et al., 2018) and graphene organic framework [Haque et al., 2017], also the CO_2 uptakes of our synthesized carbon materials are among the highest ones. Furthermore, we estimated the isosteric heats of adsorption (Q_{st}) of these N-doped mesoporous carbons from their CO_2 uptakes at 298 and 273 K,

Table 2
XPS data of N-doped mesoporous carbons prepared from self-assembled mixtures of N-resol/PEO-*b*-PCL at various N-resol concentrations.

	Wt.%			N Species				O Species				
Samples	C	N	O	N-6	N-5	N-Q	N-X	Quinone	C = O	C-O	C-OH	H_2O
50/50	79	11.5	9.5	43.77	20.87	19.70	15.64	13.27	41.30	17.42	12.54	15.45
60/40	78	13	9	33.20	44.30	19.40	3.08	14.84	42.90	20.94	16.52	4.7
70/30	75	12	13	37.70	12.22	40.01	10.04	11.46	33.28	25.97	20.10	9.16

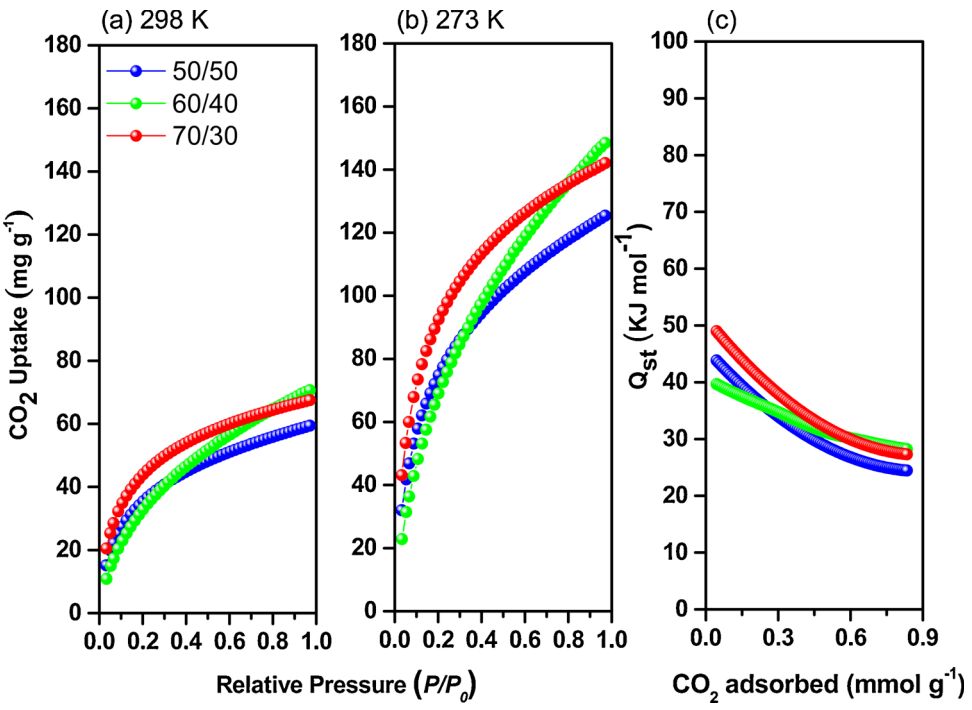

Fig. 9. (a, b) CO_2 uptake properties of N-doped mesoporous carbons obtained after calcination of self-assembled mixtures of N-resol/PEO-*b*-PCL at various N-resol concentrations (50/50, 60/40, 70/30) at (a) 298 and (b) 273 K. (c) Isosteric heats of adsorption (Q_{st}) of these N-doped mesoporous carbons, calculated from their CO_2 uptake curves at 298 and 273 K.

according to the Clausius–Clapeyron equation (Fig. 9c). The N-doped mesoporous gyroid carbon provided values of Q_{st} of 40.66 and 28.20 kJ mol^{-1} at low and high adsorptions of CO_2 (ca. 0.1 and 0.8 mmol g^{-1}), respectively. The N-doped mesoporous cylinder carbon obtained from the N-resol/PEO-*b*-PCL = 50/50 system provided values of Q_{st} at low and high adsorptions of CO_2 (ca. 0.1 and 0.8 mmol g^{-1}) of 43.83 and 24.43 kJ mol^{-1}, respectively; for the sample obtained from the N-resol/PEO-*b*-PCL = 70/30 system, these values were 48.99 and 27.30 kJ mol^{-1}, respectively. These high values of Q_{st} indicate that our synthesized carbons interact very strongly with molecules of CO_2, similar to the behavior of activated carbons (Himeno et al., 2005; Keskin et al., 2010).

3.5. Dye adsorption: kinetics and reusability

It has been reported previously that the incorporation of N atoms or N-containing groups into carbon structures can dramatically enhance their adsorption efficiency toward dyes. The high charge density of N atoms can create more basic sites on the carbon surface and, thereby, enhance the interactions between the carbon materials and cationic dyes through various types of noncovalent interactions (e.g., electrostatic, dipole–dipole). In addition, carbon structures having large pore volumes, high surface areas, and hydrophobic characteristics have greater ability to function as potential adsorbents for small molecules (Ben et al., 2009). Accordingly, we tested the suitability of our synthesized N-doped mesoporous materials for use as adsorbents for water-treatment by evaluating their adsorption efficiencies toward organic dyes. Because it featured the highest N atom content, the largest pore volume, and the greatest surface area, we examined the N-doped mesoporous gyroid carbon (formed from the N-resol/PEO-*b*-PCL = 60/40 system) for the removal of RhB and MO from water. For quantitative assessment of the adsorption of this N-doped mesoporous gyroid carbon, we monitored the dye adsorption processes by measuring the UV–Vis spectra of the aqueous dye solutions at various times (from 0 to 9 min) after the addition of the carbon material. For RhB, the supernatants of the dye/carbon solutions were separated at various times and their UV–Vis spectra were recorded (Fig. 10A). The intensity of the absorbance peak at (λ_{max}) of 554 nm decreased gradually upon increasing the time from 0 to 45 min, and disappeared completely within 60 min. The inset to Fig. 10B presents photographs of the supernatant of the dye/carbon solution at various times; the color of the aqueous dye solution changed from deep-red/violet to colorless within 60 min. Thus, our synthesized N-doped mesoporous gyroid carbon displayed high efficiency for the removal of RhB from water; the maximum removal efficiency of RhB (98 %) was very fast, within 60 min (Fig. 10B). Similarly, for MB, we separated the supernatants of the dye/carbon solutions at various times and recorded their UV–Vis spectra. As displayed in Fig. 10C, the intensity of the absorbance peak at (λ_{max}) 664 nm decreased over the period from 0 to 30 min and disappeared completely within 45 min. In addition, photographs of the isolated supernatants from the dye/carbon solutions revealed a color change from deep-blue to colorless within 45 min, as revealed in the inset to Fig. 10D. Thus, our synthesized N-doped mesoporous gyroid carbon also displayed high efficiency for the removal of MB from water. Fig. 10D reveals that the maximum removal efficiency of MB (98 %) occurred within 45 min.

To further examine the adsorption behavior of the dyes RhB and MO on the surface of the N-doped mesoporous gyroid carbon, we applied the Langmuir isothermal mode (Langmuir, 1918) to fit the equilibrium adsorption data. As summarized in Table 3, the fitting data provided correlation coefficients (R_L^2) of the Langmuir isotherm model of 0.93701 for RhB and 0.99797 for MB (Fig. 11A). Based on the Langmuir equation, the maximum adsorption capacities (Q_m) of the N-doped mesoporous gyroid carbon toward RhB and MO were 204.08 and 308.64 mg g^{-1}, respectively (Fig. 11B). We attribute the higher value of Q_m for MO, relative to that for RhB, to the smaller size of the MB dye. Furthermore, a comparison of the values of Q_m for the N-doped mesoporous gyroid carbon with those of previously reported N-doped carbons confirmed that our synthesized N-doped mesoporous gyroid carbon is one of the strongest adsorbent materials for dye removal from water (Table 4). In comparison with mesoporous carbons, the ordered mesoporous carbon which prepared using soft template of triblock copolymer (Pluronic P123) exhibited adsorption values (Q_m) of 83 and 196 mg g^{-1} for rhodamine B and MB, respectively (Jedynak et al., 2019; Yuan et al., 2007), indicating that the doping of nitrogen in the mesoporous carbons significant enhanced their adsorption efficiencies of dyes (Table 4). Furthermore, we used cyclic adsorption-regeneration tests of aqueous RhB and MO dye solutions to examine the reusability of our N-doped mesoporous gyroid carbon. As displayed in Figs. 11C and

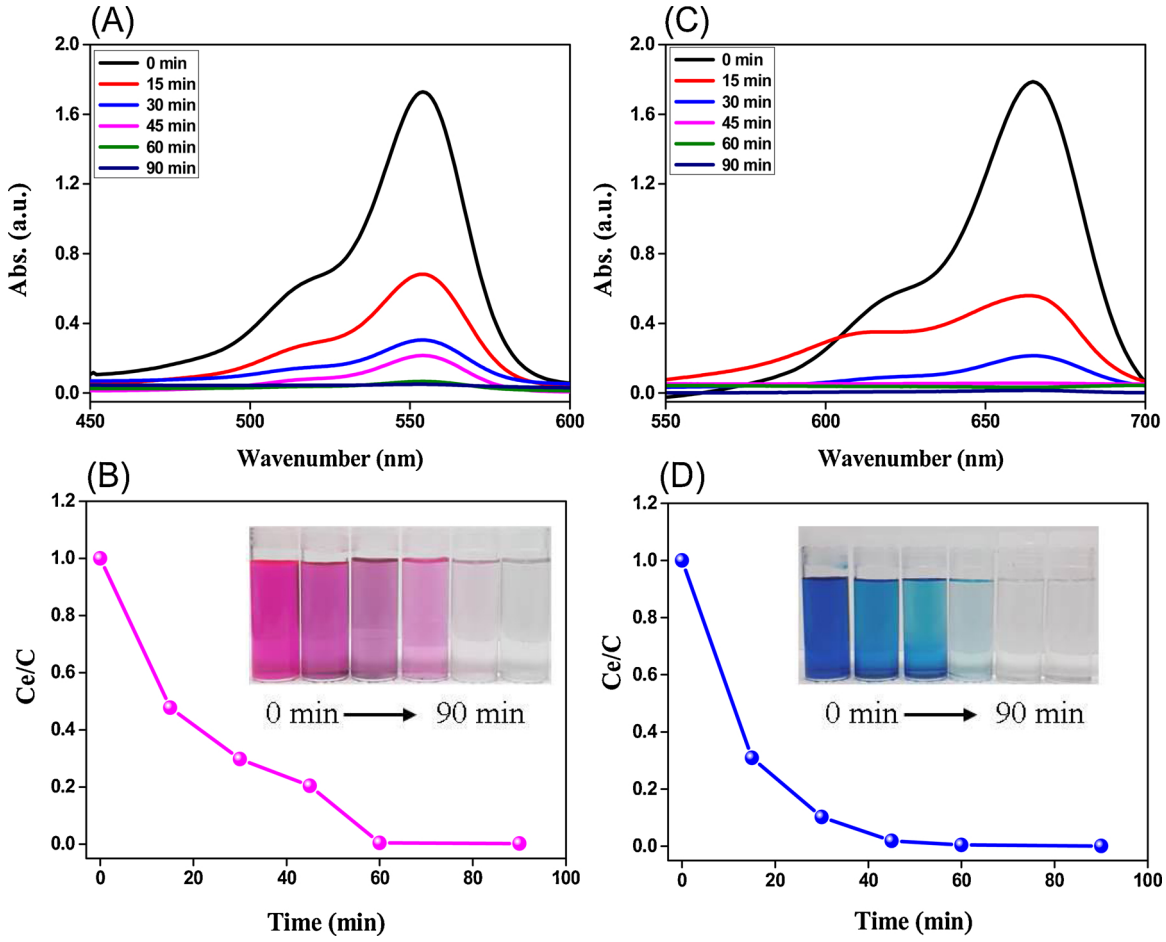

Fig. 10. (A, B) UV–Vis spectra of aqueous (A) RhB and (B) MB solutions recorded at various time periods after the addition of the N-doped mesoporous gyroid carbon (initial concentration of both RhB and MB: 25 mg L^{-1}). (C, D) Adsorption rates of (C) RhB and (D) MO [initial concentration (*C*): 25 mg L^{-1}] on the N-doped mesoporous gyroid carbon at various periods of time. Insets: Corresponding photographs.

Table 3
Fitted parameters for the adsorptions of RhB and MB on the N-doped mesoporous gyroid carbon, obtained using the Langmuir adsorption isothermal model.

	Q_m (mg g^{-1})	K_L	R_L^2
RhB	204.08	0.1660	0.93701
MO	308.64	0.7058	0.99797

11D, the adsorption efficiencies of this N-doped mesoporous gyroid carbon toward RhB and MO both decreased only negligibly after five regeneration cycles, suggesting that our synthesized carbon material could, indeed, be applied as an efficient adsorbent for the removal of dyes from wastewater.

The mechanism of dye adsorption on carbon materials has been previously reported, indicating that the adsorption process can be happened through electrostatic interaction between negative sites on carbon and positive charges of dye molecules, acid-base interaction between N−H group on carbon and COOH groups of dye molecules, and π-π stacking interaction between aromatic rings in carbon and dye molecules (Wang et al., 2019; Tripathi et al., 2013; Ezzeddine et al., 2016). In order to investigate the adsorption mechanism of rhodamine B and MB on our prepared N-doped mesoporous gyroid carbon, FTIR analyses of rhodamine, MB, carbon before and after dye adsorption were measured, as shown in Fig. S8. FTIR spectrum of rhodamine dye characterized by a broad signal at 3404 cm^{-1}, representing the stretching of carboxylic COOH group, in addition to two signals at 1590 and 1469 cm^{-1}, representing the vibrations of aromatic C=C bonds (Fig. S8A). After adsorption process, there no significant change in the signals except some shifting in the signals of carboxylic COOH group and aromatic C=C bonds to 3335, 1582, and 1462 cm^{-1}, indicating the presence of acid-base and π-π stacking interactions between N-doped mesoporous gyroid carbon and rhodamine B dye (Fig. S8C). On the other hand, FTIR spectrum of MB featured by two signals at 1600 and 1493 cm^{-1}, representing the vibrations of aromatic C=C bonds in addition to signal at 1484 cm^{-1} for the CS= bond (Fig. S8B). After adsorption process, also there no significant change in the signals except some shifting in the signals of aromatic C=C and CS= bonds to 1591, 1478, and 1170 cm^{-1}, respectively, indicating he presence of π-π stacking and electrostatic interactions between N-doped mesoporous gyroid carbon and MB dye (Fig. S8C).

4. Conclusions

We have prepared a novel N-resol through the simple condensation of THPT and formaldehyde in the presence of NaOH as a catalyst. We then prepared a series of self-assembled N-resol/PEO-*b*-PCL systems and resultant N-doped mesoporous carbons having various mesophase structures, including cylindrical and gyroid, through the soft-templated method. The N-doped mesoporous gyroid carbon (obtained from the N-resol/PEO-b-PCL = 60/40 system) exhibited a high N atom content (13 %), while the two N-doped mesoporous cylinder carbons possessed N atom contents of 11.5–12 %. The synthesized N-doped mesoporous carbons displayed excellent CO_2 uptake efficiencies of up to 72 and 150 mg g^{-1} at 298 and 273 K, respectively. Because it had the highest N

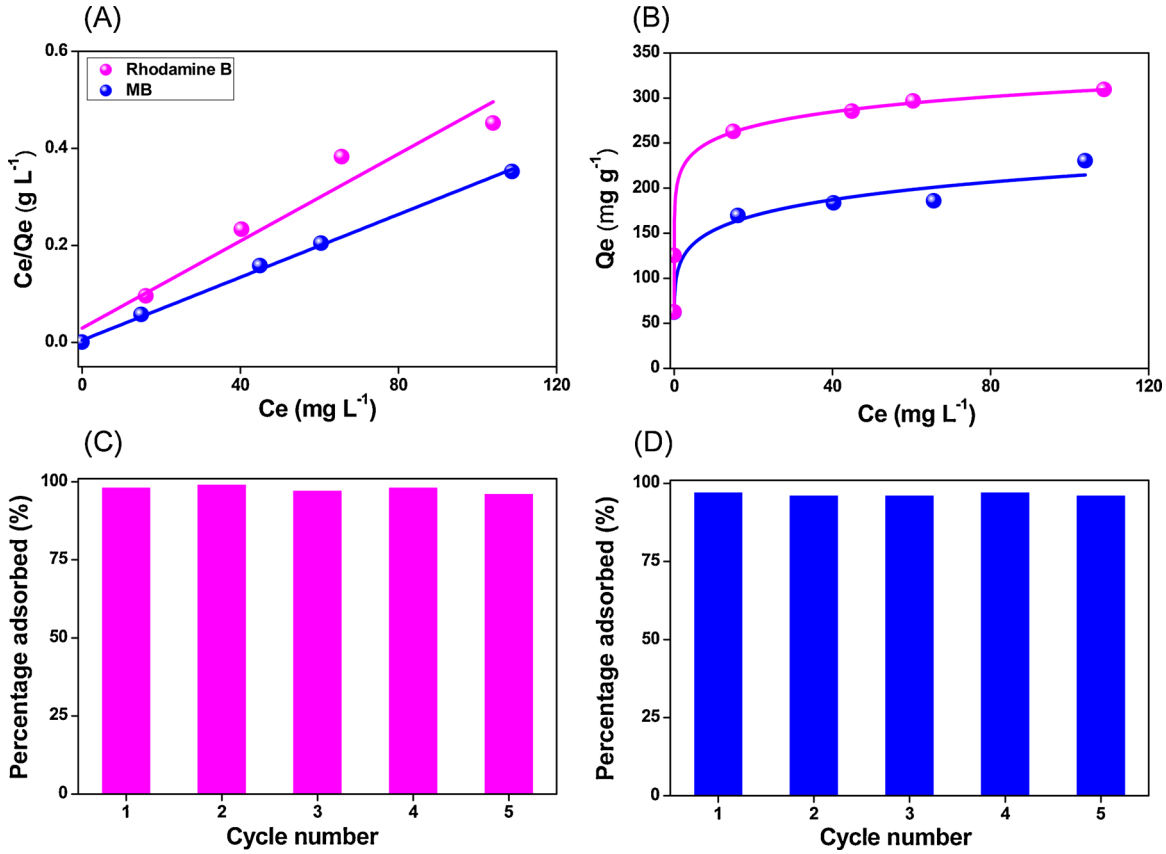

Fig. 11. (A) Langmuir isothermal models and (B) adsorption isothermal curves for the adsorption of the dyes RhB and MB (initial concentration: 25 mg L^{-1}) on the N-doped mesoporous gyroid carbon. (C, D) Reusability of the N-doped mesoporous gyroid carbon for the removal of (C) RhB and (D) MB within 60 min.

Table 4
Maximum adsorption capacities of RhB or MB on the N-doped mesoporous gyroid carbon structure, compared with those of other reported carbon materials.

Adsorbent	Dye	Q_m (mg g^{-1})	Ref.
Graphene sponge	RhB	72.5	Zhao et al. (2012)
Nanoporous PDVB-VI-0.2	RhB	260.4	Han et al. (2015)
S1	RhB	200	Wang et al. (2017)
Graphene nanosheet	MB	111.6	Fan et al. (2011)
Ultrathin-shell BN hollow sphere	MB	191.7	Lian et al. (2012)
Hollow octahedral carbon cage	MB	198.9	Aijaz et al. (2015)
Well-defined microporous carbon	MB	292	Li et al. (2014)
CNF 127	MB	73	Kundu et al. (2018)
Mesoporous carbon (ST-A)	RhB	83	Jedynak et al. (2019)
Mesoporous carbon (OMC-100)	MB	196	Yuan et al. 2007
N-doped mesoporous gyroid carbon	RhB	**204.08**	**This work**
N-doped mesoporous gyroid carbon	MB	**308.64**	**This work**

atom content (13 %), the largest pores (23 nm), and the highest mesoporous volume ratio (74.78 %), the N-doped mesoporous double-gyroid carbon structure exhibited very high adsorption capacities toward the organic dyes RhB and MB in water: 204.08 and 308.64 mg g^{-1}, respectively; furthermore, these maximum adsorption capacities were achieved within very short periods of time (up to 45 min). Accordingly, we suspect that our new triazine-based N-resol has great suitability for use in the simple preparation of various kinds of N-doped mesoporous carbons having additional potential applicability in, for example, catalysis, sensors, and energy storage.

Credit author statement

Ahmed F. M. EL-Mahdy: Design the experiment, methodology and writing. **Tzu-En Liu**: Did the experiment and writing. **Shiao-Wei Kuo**: Analysis of the data, literature review and writing this paper.

Author contributions

All authors were involved all the study. A.E. and T.E.L designed the experiments and analyzed the data. A.E. and S.W.K conducted experiments and wrote the manuscript. All authors approve the final version of the manuscript.

Declaration of Competing Interest

The authors declare that they have no known competing financial interests or personal relationships that could have appeared to influence the work reported in this paper.

Acknowledgments

This study was supported financially by Ministry of Science and Technology, Taiwan, under contracts MOST 106-2221-E-110- 067-MY3, 108-2638-E-002-003-MY2, 108-2218-E-110-013-MY3, and 108-2221-E-110-014-MY3.

Appendix A. Supplementary data

Supplementary material related to this article can be found, in the online version, at doi:https://doi.org/10.1016/j.jhazmat.2020.122163.

References

Chen, A.B., Yu, Y.F., Wang, R.J., Yu, Y.H., Zang, W.W., Tang, P., Ma, D., 2015. Nitrogen-doped dual mesoporous carbon for the selective oxidation of ethylbenzene. Nanoscale

7, 14684–14690. https://doi.org/10.1039/C5NR03802B.
Abuzeid, H.R., EL-Mahdy, A.F.M., Ahmed, M.M.M., Kuo, S.W., 2019. Triazine-functionalized covalent benzoxazine framework for direct synthesis of N-doped microporous carbon. Polym. Chem. 10, 6010–6020. https://doi.org/10.1039/C9PY01231A.
Adeyemo, A.A., Adeoye, I.O., Bello, O.S., 2012. Metal organic frameworks as adsorbents for dye adsorption: overview, prospects and future challenges. Toxicol. Environ. Chem. 94, 1846–1863. https://doi.org/10.1080/02772248.2012.744023.
Aijaz, A., Sun, J.K., Pachfule, P., Uchida, T., Xu, Q., 2015. From a metal–organic framework to hierarchical high surface-area hollow octahedral carbon cages. Chem. Commun. 51, 13945–13948. https://doi.org/10.1039/C5CC04230E.
Allen, S.J., Koumanova, B., 2005. Decolourisation of water/wastewater using adsorption. J. Univ. Chem. Technol. Metall. 40, 175–192.
Bai, F., Xia, Y., Chen, B., Su, H., Zhu, Y., 2014. Preparation and carbon dioxide uptake capacity of N-doped porous carbon materials derived from direct carbonization of zeolitic imidazolate framework. Carbon 79, 213–226. https://doi.org/10.1016/j.carbon.2014.07.062.
Bayatsarmadi, B., Zheng, Y., Jaroniec, M., Qiao, S.Z., 2015. Soft-templating synthesis of N-Doped mesoporous carbon nanospheres for enhanced oxygen reduction reaction. Chem. Asian J. 10, 1546–1553. https://doi.org/10.1002/asia.201500287.
Ben, T., Ren, H., Ma, S., Cao, D., Lan, J., Jing, X., Wang, W., Xu, J., Deng, F., Simmons, J.M., Qiu, S., Zhu, G., 2009. Targeted Synthesis of a porous aromatic framework with high stability and exceptionally high surface area. Angew. Chem., Int. Ed. 48, 9457–9460. https://doi.org/10.1002/anie.200904637.
Chen, W.C., Kuo, S.W., Lu, C.H., Jeng, U.S., Chang, F.C., 2009. Self-assembly structures through competitive interactions of crystalline − amorphous diblock copolymer/homopolymer blends: poly(ε-caprolactone-b-4-vinylpyridine)/Poly(vinylphenol). Macromolecules 42, 3580–3590. https://doi.org/10.1021/ma900080v.
Chen, L.F., Zhang, X.D., Liang, H.W., Kong, M., Guan, Q.F., Chen, P., Wu, Z.Y., Yu, S.H., 2012. Synthesis of nitrogen-doped porous carbon nanofibers as an efficient electrode material for supercapacitors. ACS Nano 6, 7092–7102. https://doi.org/10.1021/nn302147s.
Chu, W.C., Lin, C.X., Kuo, S.W., 2014. Solvent-tuning of ordered mesoporous silicas prepared through evaporation-induced self-assembly templated by poly(ethylene oxide-*b*-ε-caprolactone). RSC Adv. 4, 61012–61021. https://doi.org/10.1039/c4ra11569d.
Chu, W.C., D, L, Chen, J.K., Huang, C.F., Kuo, S.W., 2016. Tunable mesoporous phenolic-silica composites templated by poly(ethylene oxide-b-caprolactone) block copolymer. J. Nanosci. Nanotechnol. 16, 9085–9092. https://doi.org/10.1166/jnn.2016.12909.
Chu, W.C., Bastakoti, B.P., Kaneti, Y.V., Li, J.G., Alamri, H.R., Alothman, Z.A., Yamauchi, Y., Kuo, S.W., 2017. Tailored design of bicontinuous gyroid mesoporous carbon and nitrogen-doped carbon from poly(ethylene oxide-b-caprolactone) diblock copolymers. Chem. Eur. J. 23, 13734–13741. https://doi.org/10.1002/chem.201702360.
Deng, Y., Xie, Y., Zoua, K., Ji, X., 2016. Review on recent advances in nitrogen-doped carbons: preparations and applications in supercapacitors. J. Mater. Chem. A Mater. Energy Sustain. 4, 1144–1173. https://doi.org/10.1039/C5TA08620E.
Dong, Y., Lin, H., Jin, Q., Li, L., Wang, D., Zhou, D., Qu, F., 2013. Synthesis of mesoporous carbon fibers with a high adsorption capacity for bulky dye molecules. J. Mater. Chem. 1, 7391–7398. https://doi.org/10.1039/C3TA10787F.
Dutta, S., Bhaumik, A., Wu, K.C.-W., 2014. Hierarchically porous carbon derived from polymers and biomass: effect of interconnected pores on energy applications. Energy Environ. Sci. 7, 3574–3592. https://doi.org/10.1039/C4EE01075B.
Dutta, S., Kim, J., Ide, Y., Kim, J.H., Hossain, Md.S.A., Bando, Y., Yamauchi, Y., Wu, K.C.-W., 2017. 3D network of cellulose-based energy storage devices and related emerging applications. Mater. Horiz. 4, 522–545. https://doi.org/10.1039/c6mh00500d.
El-Mahdy, A.F.M., Kuo, C.H., Alshehri, A., Young, C., Yamauchi, Y., Kim, J., Kuo, S.W., 2018. Strategic design of triphenylamine-and triphenyltriazine-based two-dimensional covalent organic frameworks for CO 2 uptake and energy storage. J. Mater. Chem. A. 6 (40), 19532–19541. https://doi.org/10.1039/C8TA04781B.
EL-Mahdy, A.F.M., Hung, Y.H., Mansoure, T.H., Yu, H.H., Hsu, Y.S., Wu, K.C.-W., Kuo, S.W., 2019a. Synthesis of [3+ 3] β-ketoenamine-tethered covalent organic frameworks (COFs) for high-performance supercapacitance and CO2 storage. J. Taiwan Inst. Chem. E. 103, 199–208. https://doi.org/10.1016/j.jtice.2019.07.016.
EL-Mahdy, A.F.M., Young, C., Kim, J., You, J., Yamauchi, Y., Kuo, S.W., 2019b. Hollow microspherical and microtubular [3+ 3] carbazole-based covalent organic frameworks and their gas and energy storage applications. ACS Appl. Mater. Interfaces 11 (9), 9343–9354. https://doi.org/10.1021/acsami.8b21867.
Ezzeddine, Z., Batonneau-Gener, I., Pouilloux, Y., Hamad, H., 2016. Removal of methylene blue by mesoporous CMK-3: kinetics, isotherms and thermodynamics. J. Mol. Liq. 223, 763–770. https://doi.org/10.1016/j.molliq.2016.09.003.
Fan, Z.J., Kai, W., Yan, J., Wei, T., Zhi, L.J., Feng, J., Ren, Y.M., Song, L.P., Wei, F., 2011. Facile synthesis of graphene nanosheets via Fe reduction of exfoliated graphite oxide. ACS Nano 5, 191–198. https://doi.org/10.1021/nn102339t.
Forgacs, E., Cserháti, T., Oros, G., 2004. Removal of synthetic dyes from wastewaters: a review. Environ. Int. 30, 953–971. https://doi.org/10.1016/j.envint.2004.02.001.
Gu, L., Zhu, N., Guo, H., Huang, S., Lou, Z., Yuan, H., 2013. Adsorption and fenton-like degradation of naphthalene dye intermediate on sewage sludge derived porous carbon. J. Hazard. Mater. 246–247, 145–153. https://doi.org/10.1016/j.jhazmat.2012.12.012.
Guo, S.N., Shen, H.K., Tie, Z.F., Zhu, S., Shi, P.H., Fan, J.C., Xu, Q.J., Min, Y.L., 2017. Three-dimensional cross-linked Polyaniline fiber/N-doped porous carbon with enhanced electrochemical performance for high-performance supercapacitor. J. Power Sources 359, 285–294. https://doi.org/10.1016/j.jpowsour.2017.04.100.
Gupta, V.K., Suhas, 2009. Application of low-cost adsorbents for dye removal – a review. J. Environ. Manage. 90, 2313–2342. https://doi.org/10.1016/j.jenvman.2008.11.017.
Han, Y., Li, W., Zhang, J., Meng, H., Xu, Y., Zhang, X., 2015. Adsorption behavior of rhodamine B on nanoporous polymers. RSC Adv. 5, 104915–104922. https://doi.org/10.1039/C5RA21130A.
Hao, G.P., Li, W.C., Qian, D., Lu, A.H., 2010. Rapid synthesis of nitrogen-doped porous carbon monolith for CO_2 capture. Adv. Mater. 22 (853-), 857. https://doi.org/10.1002/adma.200903765.
Haque, E., Islam, M., Pourazadi, E., Sarkar, S., Harris, A.T., Minett, A.I., Yanmaz, E., Alshehri, S.M., Ide, Y., Wu, K.C.-W., Kaneti, Y.V., Yamauchi, Y., Hossain, M.A., 2017. Boron-functionalized graphene oxide-organic frameworks for highly efficient CO_2 capture. Chem. Asian J. 12, 283–288. https://doi.org/10.1002/asia.201601442.
Himeno, S., Komatsu, T., Fujita, S., 2005. High-pressure adsorption equilibria of methane and carbon dioxide on several activated carbons. J. Chem. Eng. Data 50, 369–376. https://doi.org/10.1021/je049786x.
Hu, D., Xu, Z., Zeng, K., Zheng, S., 2010. From self-organized novolac resins to ordered nanoporous carbons. Macromolecules 43, 2960–2969. https://doi.org/10.1021/ma902770r.
Jedynak, K., Wideł, D., Redzia, N., 2019. Removal of rhodamine B (a basic dye) and acid yellow 17 (an acidic dye) from aqueous solutions by ordered mesoporous carbon and commercial activated carbon. Colloids Interfaces 3, 30. https://doi.org/10.3390/colloids3010030.
Jiao, Y., Xu, L., Sun, H., Deng, Y., Zhang, T., Liu, G., 2017. Synthesis of benzxazine-based nitrogen-doped mesoporous carbon spheres for methyl orange dye adsorption. J. Porous Mater. 24, 1565–1574. https://doi.org/10.1007/s10934-017-0396-z.
Kaneti, Y.V., Dutta, S., Hossain, Md.S.A., Shiddiky, M.J.A., Tung, K.L., Shieh, F.-K., Tsung, C.-K., Wu, K.C.-W., Yamauchi, Y., 2017. Strategies for improving the functionality of zeolitic imidazolate frameworks: tailoring nanoarchitectures for functional applications. Adv. Mater. 29, 1700213. https://doi.org/10.1002/adma.201700213.
Keskin, S., van Heest, T.M., Sholl, D.S., 2010. Can metal–organic framework materials play a useful role in large-scale carbon dioxide separations. Chem. Sus. Chem. 3, 879–891. https://doi.org/10.1002/cssc.201000114.
Kosonen, H., Ruokolainen, J., Torkkeli, M., Serimaa, R., Nyholm, P., Ikkala, O., 2002. Micro- and macrophase separation in phenolic resol resin/PEO-PPO-PEO block copolymer blends: effect of hydrogen-bonded PEO length. Macromol. Chem. Phys. 203, 388–392. https://doi.org/10.1002/1521-3935(20020101)203:2<388::AID-MACP388>3.0.CO,2-K.
Kundu, S., Chowdhury, I.H., Naskar, M.K., 2018. Nitrogen-doped nanoporous carbon Nanospheroids for selective dye adsorption and Pb(II) ion removal from waste water. ACS Omega 3, 9888–9898. https://doi.org/10.1021/acsomega.8b01252.
Kuo, S.W., 2018. Hydrogen Bonding in Polymeric Materials. Wiley-VCH, Weinheim, Germany. https://doi.org/10.1002/9783527804276.
Kuo, S.W., Lin, C.L., Chang, F.C., 2002. Phase behavior and hydrogen bonding in ternary polymer blends of phenolic resin/poly(ethylene oxide)/poly(ε-caprolactone). Macromolecules 35, 278–285. https://doi.org/10.1021/ma011255f.
Langmuir, I., 1918. The adsorbtion of gases on plane surfaces of glass mica and platinum. J. Am. Chem. Soc. 40, 1361–1403. https://doi.org/10.1021/ja02242a004.
Lee, J., Kim, J., Hyeon, T., 2006. Recent progress in the synthesis of porous carbon materials. Adv. Mater. 18, 2073–2094. https://doi.org/10.1002/adma.200501576.
Lee, J.H., Park, N., Kim, B.G., Jung, D.S., Im, K., Hur, J., Choi, J.W., 2013. Restacking-inhibited 3D reduced graphene oxide for high performance supercapacitor electrodes. ACS Nano 7, 9366–9374. https://doi.org/10.1021/nn4040734.
Lee, H.C., Hsueh, H.Y., Jeng, U.S., Ho, R.M., 2014. Functionalized nanoporous gyroid SiO_2 with double-stimuli-responsive properties as environment-selective delivery systems. Macromolecules 47, 3041–3051. https://doi.org/10.1021/ma500360a.
Li, J.G., Kuo, S.W., 2011. Phase behavior of mesoporous nanostructures templated by amphiphilic crystalline–crystalline diblock copolymer of poly(ethylene oxide-b-ε-caprolactone). RSC Adv. 1, 1822–1833. https://doi.org/10.1039/C1RA00349F.
Li, J.G., Lin, Y.D., Kuo, S.W., 2011. From microphase separation to self-organized mesoporous phenolic resin through competitive hydrogen bonding with double-crystalline diblock copolymers of poly(ethylene oxide-*b*-ε-caprolactone). Macromolecules 44, 9295–9309. https://doi.org/10.1021/ma2010734.
Li, Z., Wu, D., Liang, Y.F.R., Matyjaszewski, K., 2014. Synthesis of well-defined microporous carbons by molecular-scale templating with polyhedral oligomeric silsesquioxane moieties. J. Am. Chem. Soc. 136, 4805–4808. https://doi.org/10.1021/ja412192v.
Li, H., An, N., Liu, G., Li, J., Liu, N., Jia, M., Zhang, W., Yuan, X., 2016. Adsorption behaviors of methyl orange dye on nitrogen-doped mesoporous carbon materials. J. Colloid Interface Sci. 466, 343–351. https://doi.org/10.1016/j.jcis.2015.12.048.
Li, Y., Kim, J., Wang, J., Liu, N.L., Bando, Y., Alshehri, A.A., Yamauchi, Y., Hou, C.H., Wu, K.C.-W., 2018. High performance capacitive deionization using modified ZIF-8-derived, N-doped porous carbon with improved conductivity. Nanoscale 10, 14852–14859. https://doi.org/10.1039/C8NR02288G.
Li, J.G., Ho, Y.F., Ahmed, M.M.M., Liang, H.C., Kuo, S.W., 2019. Mesoporous carbons templated by PEO-PCL block copolymers as electrode materials for supercapacitors. Chem. Eur. J. 25, 10456–10463. https://doi.org/10.1002/chem.201901724.
Lian, G., Zhang, X., Zhang, S.J., Liu, D., Cui, D.L., Wang, Q.L., 2012. Controlled fabrication of ultrathin-shell BN hollow spheres with excellent performance in hydrogen storage and wastewater treatment. Energy Environ. Sci. 5, 7072–7080. https://doi.org/10.1039/C2EE03240F.
Liang, C.D., Li, Z.J., Dai, S., 2008. Mesoporous carbon materials: synthesis and modification. Angew. Chem. Int. Ed. 47, 3696–3717. https://doi.org/10.1002/anie.200702046.
Liang, T., Wang, F., Liang, L., Liu, M., Sun, J., 2016. Magnetically separable nitrogen-doped mesoporous carbon with high adsorption capacity. J. Mater. Sci. 51, 3868–3879. https://doi.org/10.1007/s10853-015-9706-5.
Liu, C.C., Chu, W.C., Li, J.G., Kuo, S.W., 2014a. Mediated competitive hydrogen bonding form mesoporous phenolic resins templated by poly(ethylene oxide-b-ε-caprolactone-b-l-lactide) triblock copolymers. Macromolecules 47, 6389–6400. https://doi.org/10.

1021/ma501246j.
Liu, Y., Cui, G., Luo, C., Zhang, L., Guo, Y., Yan, S., 2014b. Synthesis, characterization and application of amino-functionalized multi-walled carbon nanotubes for effective fast removal of methyl orange from aqueous solution. RSC Adv. 4, 55162–55172. https://doi.org/10.1039/C4RA10047F.
Liu, L., Xie, Z.H., Deng, Q.F., Hou, X.X., Yuan, Z.Y., 2017. One-pot carbonization enrichment of nitrogen in microporous carbon spheres for efficient CO_2 capture. J. Mater. Chem. A Mater. Energy Sustain. 5, 418–425. https://doi.org/10.1039/C6TA09782K.
Liu, Y., Wang, Z.R., Teng, W., Zhu, H.W., Wang, J.X., Elzatahry, A., Al-Dahyan, D., Li, W., Deng, Y.H., Zhao, D.Y., 2018a. A template-catalyzed in situ polymerization and co-assembly strategy for rich nitrogen-doped mesoporous carbon. J. Mater. Chem. A Mater. Energy Sustain. 6, 3162–3170. https://doi.org/10.1039/C7TA10106F.
Liu, Y., Wang, Z., Teng, W., Zhu, H., Wang, J., Elzatahry, A., Al-Dahyan, D., Li, W., Deng, Y., Zhao, D., 2018b. A Template-catalyzed in-situ polymerization and co-assembly strategy for rich Nitrogen-doped mesoporous carbon. J. Mater. Chem. A Mater. Energy Sustain. 6, 3162–3170. https://doi.org/10.1039/C7TA10106F.
Lu, Y.S., Bastakoti, B.P., Pramanik, M., Yamauchi, Y., Kuo, S.W., 2016. Direct assembly of mesoporous silica functionalized with polypeptides for efficient dye adsorption. Chem. Eur. J. 22, 1159–1164. https://doi.org/10.1002/chem.201503679.
Lu, Y.X., Ji, C.N., Li, Y., Qu, R.J., Sun, C.M., Zhang, Y., 2018. Facile one-pot synthesis of C and g-C3N4 composites with enhanced photocatalytic activity using hydroxymethylated melamine as carbon source and soft template. Mater. Lett. 211, 78–81. https://doi.org/10.1016/j.matlet.2017.09.080.
Mezohegyi, G., van der Zee, F.P., Font, J., Fortuny, A., Fabregat, A., 2012. Towards advanced aqueous dye removal processes: a short review on the versatile role of activated carbon. J. Environ. Manage. 102, 148–164. https://doi.org/10.1016/j.jenvman.2012.02.021.
Mohammadi, N., Khani, H., Gupta, V.K., Amereh, E., Agarwal, S., 2011. Adsorption process of methyl orange dye onto mesoporous carbon material–kinetic and thermodynamic studies. J. Colloid Interface Sci. 362, 457–462. https://doi.org/10.1016/j.jcis.2011.06.067.
Mori, T., Tanaka, H., Dalui, A., Mitoma, N., Suzuki, K., Matsumoto, M., Aggarwal, N., Patnaik, A., Acharya, S., Shrestha, L.K., Sakamoto, H., Itami, K., Ariga, K., 2018. Carbon nanosheets by morphology-retained carbonization of two-dimensional assembled anisotropic carbon nanorings. Angew. Chem. Int. Ed. 57, 9679–9683. https://doi.org/10.1002/anie.201803859.
Mun, Y., Kim, M.J., Park, S.A., Lee, E., Ye, Y.J., Lee, S., Kim, Y.T., Kim, S.J., Kim, O.H., Cho, Y.H., Sung, Y.E., Lee, 2018. Soft-template synthesis of mesoporous non-precious metal catalyst with Fe-Nx/C active sites for oxygen reduction reaction in fuel cells. Appl. Catal. B 222, 191–199. https://doi.org/10.1016/j.apcatb.2017.10.015.
Panamgama, L.A., Pizzi, A., 1995. A ^{13}C-NMR analysis method for phenol-formaldehyde resin strength and formaldehyde emission. J. Appl. Polym. Sci. 55, 1007–1015. https://doi.org/10.1002/app.1995.070550705.
Peng, X., Huang, D., Odoom-Wubah, T., Fu, D., Huang, J., Qin, Q., 2014. Adsorption of anionic and cationic dyes on ferromagnetic ordered mesoporous carbon from aqueous solution: equilibrium, thermodynamic and kinetics. J. Colloid Interface Sci. 430, 272–282. https://doi.org/10.1016/j.jcis.2014.05.035.
Rafatullah, M., Sulaiman, O., Hashim, R., Ahmad, A., 2010. Adsorption of methylene blue on low-cost adsorbents: a review. J. Hazard. Mater. 177, 70–80. https://doi.org/10.1016/j.jhazmat.2009.12.047.
Rao, C.N.R., Pramoda, K., 2019. Borocarbonitrides, BxCyNz, 2D nanocomposites with novel properties. Bull. Chem. Soc. Jpn. 92, 441–468. https://doi.org/10.1246/bcsj.20180335.
Rivera-Utrilla, J., Sánchez-Polo, M., Gómez-Serrano, V., Álvarez, P.M., Alvim-Ferraz, M.C.M., Dias, J.M., 2011. Activated carbon modifications to enhance its water treatment applications. An overview. J. Hazard. Mater. 187, 1–23. https://doi.org/10.1016/j.jhazmat.2011.01.033.
Sánchez-Sánchez, Á., Suárez-García, F., Martínez-Alonso, A., Tascón, J.M.D., 2015. Synthesis, characterization and dye removal capacities of N-doped mesoporous carbons. J. Colloid Interface Sci. 450, 91–100. https://doi.org/10.1016/j.jcis.2015.02.073.
Sevilla, M., Fuertes, A.B., 2011. Sustainable porous carbons with a superior performance for CO_2 capture. Eng. Environ. Sci. 4, 1765–1771. https://doi.org/10.1039/C0EE00784F.
Shen, W., Fan, W., 2013. Nitrogen-containing porous carbons: synthesis and application. J. Mater. Chem. A Mater. Energy Sustain. 1, 999–1013. https://doi.org/10.1039/C2TA00028H.
Smith, S.C., Rodrigues, D.F., 2015. Carbon-based nanomaterials for removal of chemical and biological contaminants from water: a review of mechanisms and applications. Carbon 91, 122–143. https://doi.org/10.1016/j.carbon.2015.04.043.
Sojka, S.A., Wolfe, R.A., Dietz, E.A., Dannels, B.F., 1979. Carbon-13 nuclear magnetic resonance of phenolic resins. Positional isomers of bis (hydroxybenzyl) phenols and bis(hydroxyphenyl)methanes. Macromolecules 12, 767–770. https://doi.org/10.1021/ma60070a046.
Su, W.J., Tsai, F.C., Huang, C.F., Dai, L., Kuo, S.W., 2019. Flexible epoxy resins formed by blending with the diblock copolymer PEO-*b*-PCL and using a hydrogen-bonding benzoxazine as the curing agent. Polymers 11, 201. https://doi.org/10.3390/polym11020201.
Chen, T., Deng, S., Wang, B., Huang, J., Wang, Y., Yu, G., 2015. CO_2 adsorption on crab shell derived activated carbons: contribution of micropores and nitrogen-containing groups. RSC Adv. 5, 48323–48330. https://doi.org/10.1039/C5RA04937G.
Tripathi, P.K., Liu, M., Gan, L., Qian, J., Xu, Z., Zhu, D., Rao, N.N., 2013. High surface area ordered mesoporous carbon for high-level removal of rhodamine B. J. Mater. Sci. 22, 8003–8013. https://doi.org/10.1007/s10853-013-7612-2.
Tsai, W.T., Hsu, H.C., Su, T.Y., Lin, K.Y., Lin, C.M., Dai, T.H., 2007. The adsorption of cationic dye from aqueous solution onto acid-activated andesite. J. Hazard. Mater. 147, 1056–1062. https://doi.org/10.1016/j.jhazmat.2007.01.141.
Wan, L., Wang, J., Feng, C., Sun, Y., Li, K., 2015a. Synthesis of polybenzoxazine based nitrogen-rich porous carbons for carbon dioxide capture. Nanoscale 7 (6534-), 6544. https://doi.org/10.1039/C4NR07409B.
Wan, L., Wang, J., Sun, Y., Feng, C., Li, K., 2015b. Polybenzoxazine-based nitrogen-containing porous carbons for high-performance supercapacitor electrodes and carbon dioxide capture. RSC Adv. 5, 5331–5342. https://doi.org/10.1039/C4RA13637C.
Wang, S., Ng, C.W., Wang, W., Li, Q., Hao, Z., 2012. Synergistic and competitive adsorption of organic dyes on multiwalled carbon nanotubes. Chem. Eng. J. 197, 34–40. https://doi.org/10.1016/j.cej.2012.05.008.
Wang, C.C., Li, J.R., Lv, X.L., Zhang, Y.Q., Guo, G., 2014. Photocatalytic organic pollutants degradation in metal-organic frameworks. Energy Environ. Sci. 7, 2831–2867. https://doi.org/10.1039/C4EE01299B.
Wang, S., Yang, B., Liu, Y., 2017. Synthesis of a hierarchical SnS_2 nanostructure for efficient adsorption of rhodamine B dye. J. Colloid Interface Sci. 507, 225–233. https://doi.org/10.1016/j.jcis.2017.07.053.
Wang, J., Xu, Y., Ding, B., Chang, Z., Zhang, X., Yamauchi, Y., Wu, K.C.W., 2018. Confined self-assembly in two-dimensional interlayer space: monolayered mesoporous carbon nanosheets with in-plane orderly arranged mesopores and a highly graphitized framework. Angew. Chem. Int. Ed. 57, 2894–2898. https://doi.org/10.1002/anie.201712959.
Wang, Z., Wang, K., Wang, Y., Wang, S., Chen, Z., Chen, J., Fu, J., 2019. Large-scale fabrication of N-doped porous carbon nanosheets for dye adsorption and supercapacitor applications. Nanoscale 11, 8785–8797. https://doi.org/10.1039/C9NR01777A.
Wei, L., Sevilla, M., Fuertes, A.B., Mokaya, R., Yushin, G., 2012. Polypyrrole-derived activated carbons for high-performance electrical double-layer capacitors with ionic liquid electrolyte. Adv. Funct. Mater. 22, 827–834. https://doi.org/10.1002/adfm.201101866.
Wei, J., Zhou, D., Sun, Z., Deng, Y., Xia, Y., Zhao, D., 2013a. A controllable synthesis of rich nitrogen-doped ordered mesoporous carbon for CO_2 capture and supercapacitors. Adv. Funct. Mater. 23, 2322–2328. https://doi.org/10.1002/adfm.201202764.
Wei, J., Zhou, D., Sun, Z., Deng, Y., Xia, Y., Zhao, D., 2013b. A controllable synthesis of rich Nitrogen-Doped Ordered Mesoporous Carbon for CO_2 capture and supercapacitors. Adv. Funct. Mater. 23, 2322–2328. https://doi.org/10.1002/adfm.201202764.
Werstler, D.D., 1986. Quantitative ^{13}C n.m.r. Characterization of aqueous formaldehyde resins: 1. Phenol-formaldehyde resins. Polymer 27, 750–756. https://doi.org/10.1016/0032-3861(86)90135-7.
Wu, Y.C., Bastakoti, B.P., Pramanik, M., Yamauchi, Y., Kuo, S.W., 2016. Mesoporous TiO_2 thin film formed from a bioinspired supramolecular assembly. ChemistrySelect 1, 4295–4299. https://doi.org/10.1002/slct.201601164.
Yasukawa, T., Kobayashi, S., 2019. Oxygenation of styrenes catalyzed by N-doped carbon incarcerated cobalt nanoparticles. Bull. Chem. Soc. Jpn. 92, 1980–1985. https://doi.org/10.1246/bcsj.20190251.
Yu, J., Guo, M., Muhammad, F., Wang, A., Zhang, F., Qin, L., Zhu, G., 2014. One-pot synthesis of highly ordered nitrogen-containing mesoporous carbon with resorcinol-urea-formaldehyde resin for CO_2 capture. Carbon 69, 502–514. https://doi.org/10.1016/j.carbon.2013.12.058.
Yuan, X., Zhuo, S.P., Xing, W., Cui, H.Y., Dai, X.D., Liu, X.M., Yan, Z.F., 2007. Aqueous dye adsorption on ordered mesoporous carbons. J. Colloid Interface Sci. 310, 83–89. https://doi.org/10.1016/j.jcis.2007.01.069.
Zhai, Y.P., Dou, Y.Q., Liu, X.X., Park, S.S., Ha, C.S., Zhao, D.Y., 2011. Soft-template synthesis of ordered mesoporous carbon/nanoparticle nickel composites with a high surface area. Carbon 49, 545–555. https://doi.org/10.1016/j.carbon.2010.09.055.
Zhao, J., Ren, W., Cheng, H.M., 2012. Graphene sponge for efficient and repeatable adsorption and desorption of water contaminations. J. Mater. Chem. 22, 20197–20202. https://doi.org/10.1039/C2JM34128J.
Zhao, R., Di, H., Hui, X., Zhao, D., Wang, R., Wang, C., Yin, L., 2019. Self-assembled Ti3C2 MXene and N-rich porous carbon hybrids as superior anodes for high-performance potassium-ion batteries. Energy Environ. Sci. https://doi.org/10.1039/C9EE03250A.